Master of science in Aerospace Engineering

Trajectory optimization for space debris removal

Academic Year 2024/2025

Supervisor: **Prof. Manuela Battipede**
Co-Supervisor: **Dr. Luigi Mascolo**

Candidate:
Giuseppe Francesco Marinelli

To my loving family

Abstract

The environment surrounding us has always been a source of curiosity: humankind seeks a form of global knowledge capable of answering the doubts and questions it poses in order to explain various physical phenomena. For example, by observing the sky, it has been possible to measure the passage of time.

The desire to physically verify what has been hypothesised gave a decisive push to the space age. However, this did not only bring advantages but also caused the release of objects and pollutants into the atmosphere.

Today, we have reached a point where it is no longer possible to ignore the issue: active intervention is necessary to contain and, if possible, solve the problem.

Accidental collisions, unfortunately, only increase the presence of debris in space: this is the phenomenon known as the Kessler syndrome. Every time a collision occurs between two objects – travelling at speeds on the order of km/s – it is as if a bomb explodes, generating thousands of fragments, which behave like projectiles, drifting through space and ready to collide with other objects, thus amplifying the problem.

In this context, the aim of this research is to develop a tool that uses indirect optimisation to identify efficient trajectories that minimise fuel consumption for a satellite equipped with electric thrusters, designed to collect space debris or to reach other satellites for in-orbit servicing.

The desired trajectory is computed using a single shooting method based on the Pontryagin minimum Principle (PmP). In this way, fuel usage is limited, and the thruster operates more efficiently thanks to an autonomous switching function based on bang-bang control, which regulates thrust without having to predefine the thrusting and coasting arcs.

Table of contents

List of tables

List of figures

Acronyms

2BP	Two-Body Problem
3BP	Three-Body Problem
BC	Boundary Condition
BVP	Boundary Value Problem
CoV	Calculus of Variations
DC	Differential Corrector
DCM	Direction Cosine Matrix
EM	Earth-Moon
EME2000	Earth Mean Equator and Equinox of Epoch J2000
EoM	Equation of Motion
EP	Electric Propulsion
IM	Indirect Method
IVP	Initial Value Problem
LEO	Low-Earth Orbit
LHS	Left-Hand Side
MPBVP	Multi-Point Boundary Value Problem
nBP	n-Body Problem
NL	Non Linear

NSL	Newton’s Second Law
OC	Optimal Control
OCP	Optimal Control Problem
OCT	Optimal Control Theory
ODE	Ordinary Differential Equation
PmP	Pontryagin’s minimum Principle
RF	Reference Frame
RHS	Right-Hand Side
RS	Reference System
SC	Spacecraft
SE	Sun-Earth
SRP	Solar Radiation Pressure
TS	Thrust Structure
TPBVP	Two-Point Boundary Value Problem
wrt	with respect to
ZEN	Zenith-East-North

Nomenclature

Symbol	Description	Value	Unit
$a, \vec{a}$	acceleration	–	km/s^2
$a_p, \vec{a}_p$	perturbing acceleration	–	km/s^2
$a_{drag}, \vec{a}_{drag}$	drag effect	–	km/s^2
$a_{J_2}, \vec{a}_{J_2}$	Earth asphericity effect	–	km/s^2
$\vec{a}_{srp}$	solar radiation pressure effect	–	km/s^2
$\vec{a}_{3b}$	lunisolar effect	–	km/s^2
a	semi-major axis (SMA)	–	km
a_H	Hohmann transfer SMA	–	km
A	surface	–	m^2
AU	Astronomical Unit	1.49597871×10^8	km
c	effective exhaust velocity	–	km/s
c	speed of light	2.99792458×10^5	km/s
C_{lm}	spherical harmonic coefficients (order l, degree m)	–	–
C_r	reflectivity coefficient	–	–
$D, \vec{D}$	drag	–	N
$e, \vec{e}$	eccentricity	–	–
$\mathcal{E}$	specific mechanical energy	–	$(km/s)^2$
E	epoch	–	UTC
g_0	standard gravitational acceleration	9.80665	m/s^2
G	universal gravitational constant	6.674302×10^{-20}	$km^3/(kg \cdot s^2)$
$h, \vec{h}$	specific angular momentum	–	–
$\mathcal{H}$	Hamiltonian	–	–
i	inclination	–	$rad - deg$
I_{sr}	solar constant (radiated power)	1367 ($1\ AU$)	W/m^2

I_{sp}		specific impulse	–	s
$\hat{I}, \hat{J}, \hat{K}$		EME2000 RF versors	–	–
J		Jacobian matrix	–	–
$\mathcal{J}$		OCP cost functional	–	–
	$\mathcal{J}^*$	OCP augmented cost functional	–	–
ℓ^*		characteristic lenght	–	km
$L, \vec{L}$		lift	–	N
m		mass	–	kg
M		mean anomaly	–	$rad - deg$
n		mean motion	–	rad/s
$\mathscr{p}$		semi-latus rectum	–	km
p		photon pressure	4.56×10^{-6} $(1AU)$	N/m^2
P_{lm}		Legendre functions (order l, degree m)	–	–
P		power	–	W
r		radius	–	km
$R_\oplus$		Earth radius	6371	km
R		Direction Cosine Matrix (DCM)	–	–
s_{lm}		spherical harmonic coefficients (order l, degree m)	–	–
SF		switching function	–	–
t		time	–	s
t^*		nondimensional time	–	–
T		thrust	–	N
	T_u, T_v, T_w	radial, tangential, out-of-plane T (ZEN RF)	–	N
$\mathcal{T}$		period	–	s
$\mathcal{T}_H$		Hohmann transfer period	–	s
u, v, w		radial tangential, normal velocity (ZEN RF)	–	km/s
$\mathcal{U}$		potential function	–	km/s^2
u		control variable	–	–

U		admissible controls	–	–
$v, \vec{v}$		velocity	–	km/s
$\mho$		Earth asphericity potential	–	km/s^2
x, y, z		cartesian coordinates	–	km
$\vec{x}$		state vector	–	–
$\vec{y}$		OCP augmented state vector	–	–
α_T		in-plane thrust angle	–	rad
β_T		out-of-plane thrust angle	–	rad
ΔV		change velocity	–	km/s
ϑ		declination angle	–	rad
$\lambda, \vec{\lambda}$		adjoint variable/vector	–	–
	$\lambda_r, \vec{\lambda}_r$	OCP position adjoint vector	–	–
	$\lambda_V, \vec{\lambda}_V$	OCP velocity adjoint vector (primer vector)	–	–
μ		specific gravitation parameter	–	km^3/s^2
	$\mu_\oplus$	Earth	398600	km^3/s^2
$\vec{\mu}$		OCP Lagrange multipliers	–	–
ν		true anomaly	–	rad
φ		right ascension angle	–	rad
φ		OCP functional Mayer term	–	–
Φ		OCP functional Lagrange term	–	–
$\vec{\chi}$		constraint vector	–	–
ω		argument of periapsis	–	rad
Ω		Right Ascension of Ascending Node	–	rad

First Chapter

Introduction

Preface

> We are committed to the safe and sustainable use of space to support humanity's ambition now and in the future. We recognise the importance of developing common standards, best practices and guidelines related to sustainable space operations alongside the need for a collaborative approach for space traffic management and coordination. We call on all nations to work together, through groups like the United Nations Committee on the Peaceful Uses of Outer Space, the International Organization for Standardization and the Inter-Agency Space Debris Coordination Committee, to preserve the space environment for future generations. [12]

This concern was explicitly raised during the G7 Leaders' Summit held in Cornwall in June 2021, where the long-term sustainability of outer space was highlighted as a global priority.

Since the launch of Sputnik in 1957, the modern space age has seen a rapid expansion of orbital activity. Today, Earth is enveloped by a dense and growing cloud of artificial objects. While many of these satellites perform essential functions – ranging from climate monitoring and natural disaster detection to global navigation and communication services – once their operational life ends or they suffer a malfunction, they often remain in orbit as inactive and unserviceable debris.

In the early years of the space era, this condition posed little concern due to the limited number of satellites in orbit. However, the situation has changed dramatically. Each year, hundreds of launches add thousands of new satellites to the existing population and the accumulation of useless objects is becoming increasingly problematic.

Beyond the risk of direct collisions with active satellites, these objects contribute to light pollution, interfere with astronomical observations, and leave residual pollutants in the upper atmosphere – even when de-orbiting solutions are employed.

This context compels a shift in how space is perceived: it must be considered a res communis, a global common accessible and beneficial to all humankind. As stated in the

1979 Moon Agreement – which expands upon principles set out in the Outer Space Treaty of 1967 – states are prohibited from altering the environmental balance of celestial bodies, a term which, in extended interpretation, includes Earth's orbital environment. For further information on the subject, please refer to [1].

Debris problem

Why should we concern ourselves with what happens in space, given the multitude of issues we already face on Earth?

Thousands of objects currently orbit the Earth, and countless more are either awaiting launch or already scheduled for deployment in the coming years. Alongside these, an ever-growing number of non-functional fragments – commonly referred to as space debris – occupy the same orbital regions. Their tracking has become a shared responsibility among international space agencies, research institutions, and specialised private operators.

But if this debris is, essentially, just discarded material, what's the real issue? Space is, after all, vast – so why worry about fragments drifting around our planet?

Indeed, the universe is unimaginably large, and in theory, there should be enough room for everyone. Yet a more pressing question arises: what if Earth's orbits became so overcrowded that they turned into high-risk zones for collisions between fast-moving objects? This scenario, once theoretical, was first outlined by NASA scientist Donald J. Kessler, giving rise to what is now known as the Kessler Syndrome. Although it may sound like science fiction, recent history suggests otherwise.

In 2009, the collision between two satellites – Iridium 33 and Cosmos 2251 – above Siberia offered the first real-world confirmation of the cascading effect predicted by Kessler, generating thousands of debris fragments. [20]

In some cases, human actions have deliberately contributed to the problem. This is particularly evident in military demonstrations involving Direct-Ascent Anti-Satellite (DA-ASAT) technologies, in which missiles are launched from Earth to destroy satellites in orbit. Notable cases include tests carried out by China (2007), the United States (2008), India (2019), and Russia (2021). China's test remains the most destructive in terms of

debris creation. While the US and Indian tests were conducted at lower altitudes – where atmospheric drag could facilitate self-cleaning over time – Russia's operation took place at an altitude dangerously close to that of the International Space Station (ISS), triggering a significant safety alert on board. [19]

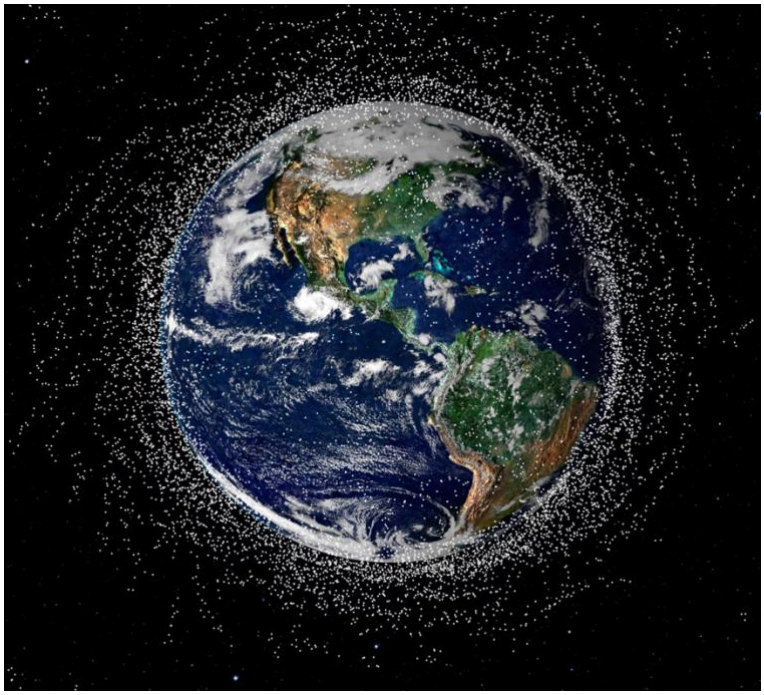

figure 1. debris distribution (credit: SCIENCE SOURCE/SCIENCE PHOTO LIBRARY)

Each object in orbit, whether operational or inactive, represents a potential ignition point in this fragile system.

Yet one might argue: if these objects ultimately burn up in the atmosphere, isn't the issue self-resolving? Won't time take care of the problem?

This is only partially true. A striking counterexample is Vanguard 1, one of the earliest artificial satellites, launched by the United States in 1958. Unlike many other spacecrafts from that era, which have since re-entered and disintegrated in the atmosphere, Vanguard 1 remains in a high Earth orbit, where atmospheric resistance is insufficient to trigger re-entry for several centuries.

Nevertheless, it is important to acknowledge the satellite's scientific legacy. Vanguard 1 contributed critical data on the shape of the Earth and the properties of the upper atmosphere. This duality highlights a broader truth: while artificial satellites are indispensable for observing both distant phenomena and Earth-bound dynamics, once

their mission ends, they must not be allowed to become hazardous remnants that threaten other active spacecraft – or worse, human life in orbit.

The number of objects in orbit is increasing exponentially, a trend clearly illustrated in the European Space Agency's Annual Space Environment Report (ESA, 2024) [11]. The urgency of implementing sustainable practices in orbital management is no longer a topic for future discussion, but a necessity for present and long-term stewardship of near-Earth space:

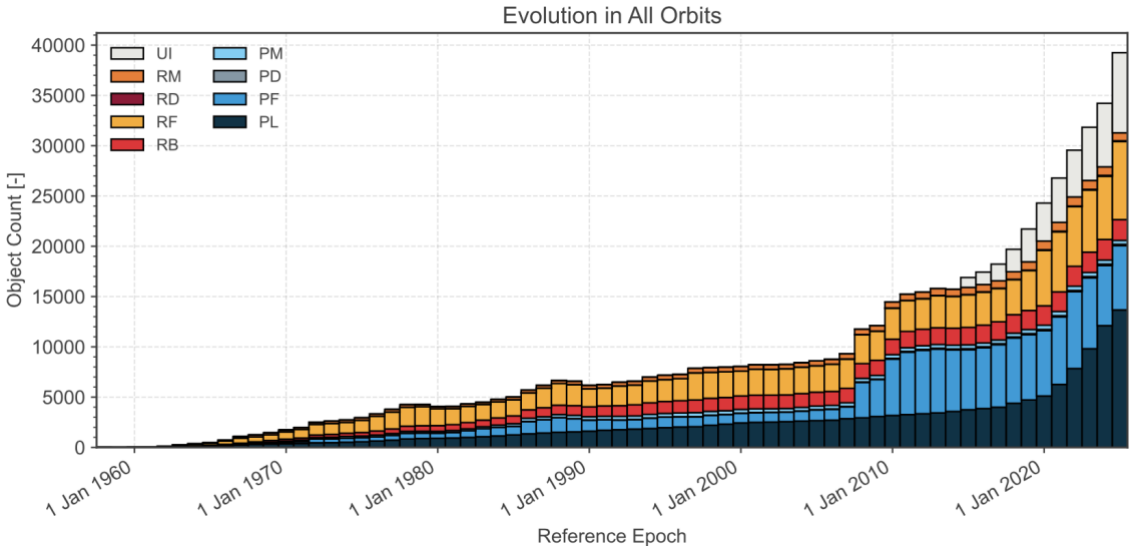

figure 2. evolution of number of objects in geocentric orbit by object class (credit: ESA)

Where:

PL	Payload
PF	Payload Fragmentation Debris
PD	Payload Debris
PM	Payload Mission Related Object
RB	Rocket Body
RF	Rocket Fragmentation Debris
RD	Rocket Debris
RM	Rocket Mission Related Object
UI	Unidentified

table 1. object classification

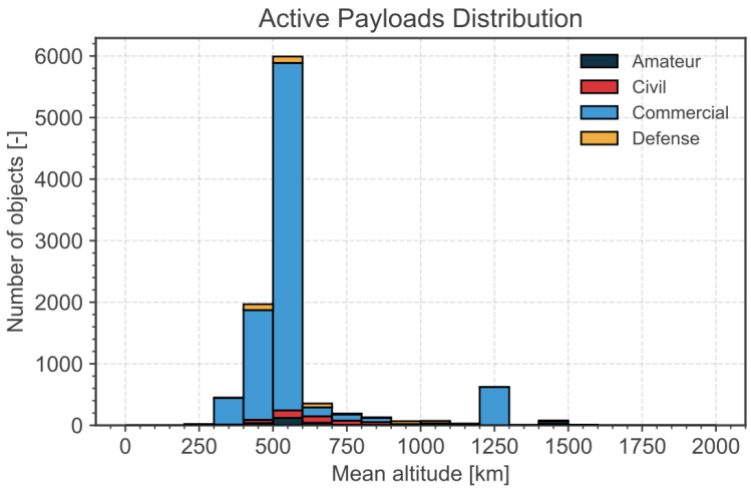

figure 3. distribution of active payloads with altitude (credit: ESA)

As shown in the figure, the distribution of active payloads with respect to altitude peaks between 500 km and 600 km.

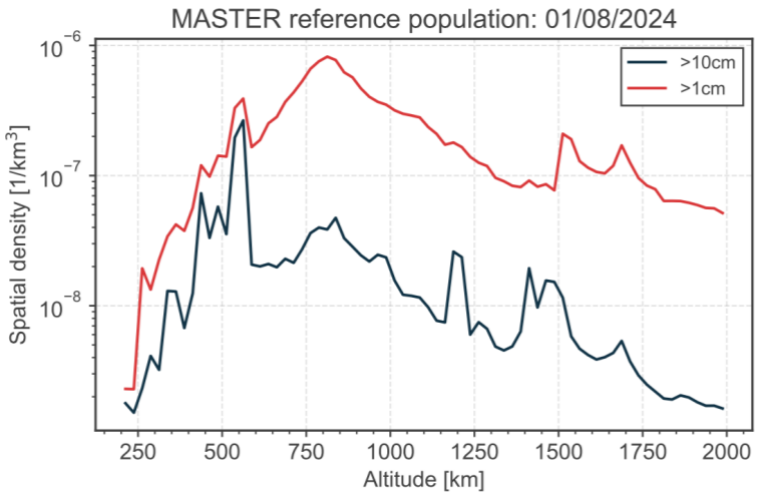

figure 4. density profiles in LEO_{IADC} for different space object size ranges from the 01/08/2024 MASTER reference population (credit: ESA)

Similarly, the distribution of objects of varying sizes reaches its peak within a slightly broader altitude range, approximately between 500 km and 1000 km.

It is evident that nano- and microsatellites are increasingly prevalent, occupying the same orbital bands where debris concentrations are also higher. This reflects a growing trend in the deployment of small-scale platforms for commercial and scientific applications – often in low Earth orbits that are already congested.

On average, 10.5 non-deliberate fragmentation events have occurred annually over the past two decades, further contributing to the accumulation of space debris.

Nevertheless, even if all launches were to cease entirely, collisions among existing debris would continue to generate new fragments, further exacerbating the situation – as illustrated in the following figure.

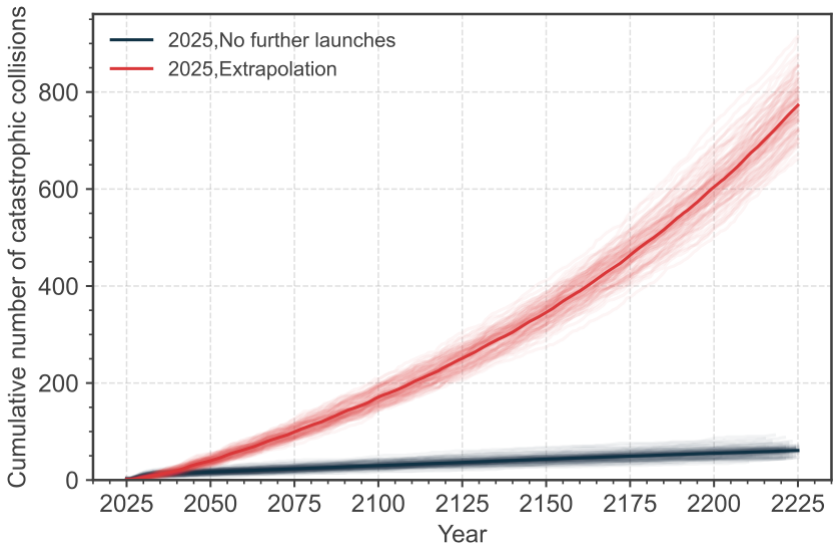

figure 5. number of cumulative collisions in LEOIADC in the simulated scenarios of long-term evolution of the environment (credit: ESA)

If further investigation is required, please go to Space debris and refer to: [13], [14], [15], [18].

Optimization methods

A satellite does not possess an infinite fuel supply: every manoeuvre entails an energy cost. One way to mitigate this constraint is using optimisation techniques that determine the most efficient trajectory for collecting debris, thereby minimising propellant consumption. These methods allow for more efficient on-board fuel management, extending mission lifetime and operational flexibility.

Such techniques are designed to adapt both temporally and spatially to the evolving characteristics of the problem. In this sense, optimised algorithms act like a real-time space navigation system, dynamically recalculating optimal paths in response to changing mission conditions.

To optimise means to find the best possible solution by varying a set of control variables – often subject to physical or operational constraints.

Most optimisation strategies employed for space trajectory design fall into three main categories: direct methods, indirect methods, and evolutionary algorithms.

The fundamental distinction between direct and indirect methods lies in how the optimal control problem is reformulated for numerical resolution.

Direct methods transform the problem into a constrained nonlinear optimisation by discretising the trajectory in both time and space. This approach requires a high number of variables to accurately capture the system dynamics. While inherently robust, direct methods often trade off precision. The strategy is primarily numerical: the trajectory and control inputs are discretised at several points, and then the algorithm searches for a set of values that minimises the objective function while satisfying all system dynamics and constraints.

Indirect methods, by contrast, are based on Pontryagin's minimum Principle (PmP). They derive the necessary conditions for optimality by solving a boundary value problem involving differential equations. The solution seeks the system's optimal behaviour and associated costates – mathematical quantities linked to the system's optimal equilibrium – by ensuring that these conditions are satisfied. Indirect methods are generally faster due to fewer variables and offer high accuracy and theoretical elegance. However, they are highly sensitive to initial guesses, which are problem-specific, and they tend to be less robust.

Finally, evolutionary algorithms are nature-inspired methods that do not rely on solving equations directly. Instead, they generate, evaluate, and evolve populations of candidate solutions, gradually converging towards optimality. These algorithms are particularly useful when the problem lacks explicit mathematical formulations. However, they are computationally intensive and offer no guaranteed convergence, making them less predictable than analytical approaches.

Dissertation overview

This paragraph contains a description and breakdown of the subsequent chapters:

- Space debris provides an in-depth analysis of space debris. The problems and causes behind its accumulation are presented, and the reasons why the current situation can no longer remain unchanged are explored. Techniques for debris removal are then proposed, along with other solutions involving the implementation of a circular economy-based model to optimise resource utilisation.
- Trajectory optimization offers an explanation of trajectory optimisation. Although treated in a preliminary and non-exhaustive manner, it provides a tool for understanding the mathematics behind the results obtained, taking into account the starting point, the destination, and everything in between.
- Dynamic model revisits essential concepts of orbital flight mechanics, including the parameters used to describe orbits, reference systems, orbital manoeuvres, and perturbations that shift the scenario from the ideal to the real case. Additionally, the dynamic models in which the satellite operates and moves over time are presented.
- The implemented OCP examines the case study in detail, dissecting it to clarify the work carried out. The results obtained are shown, and conclusions are drawn from this work, including the issues encountered, the shortcomings identified, and potential future improvements.

Second Chapter

Space debris

Introduction

Space debris refers to the collection of artificial objects orbiting the Earth that no longer serve any practical purpose.

Among this space junk are items that have been discarded or lost by those living and working in space stations, as well as fragments resulting from the breakup of rockets or satellites.

On the night of 7 August 2023, a beam of light tore through the sky above Melbourne, Australia: according to the Australian Space Agency, the glow most likely originated from the fiery remains of a Russian Soyuz-2 rocket re-entering the Earth's atmosphere. [1]

Notably, in 2024, for the first time, controlled re-entries outnumbered uncontrolled ones – a potentially promising sign of improved mitigation strategies and more responsible end-of-life planning in satellite missions. [11]

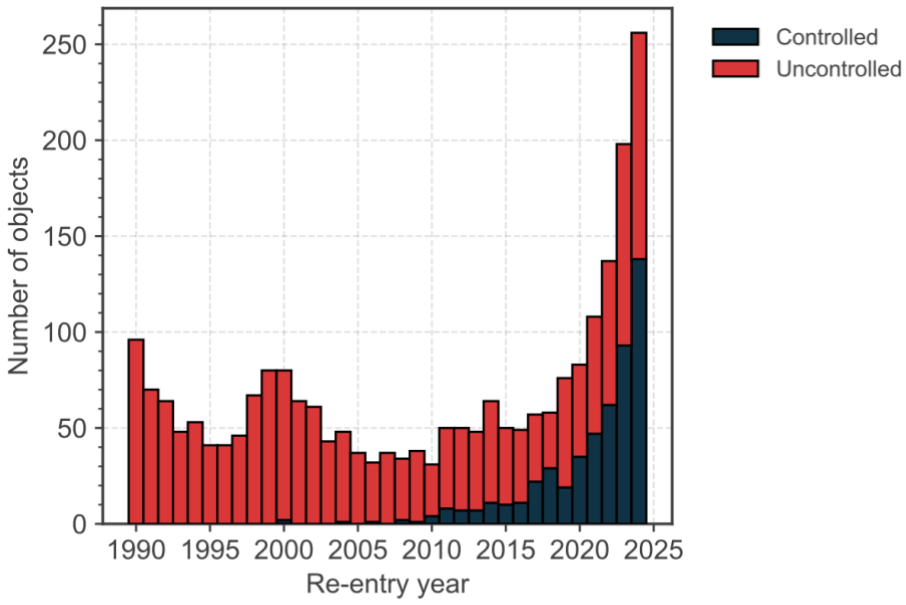

(a) Rocket Bodies: Count

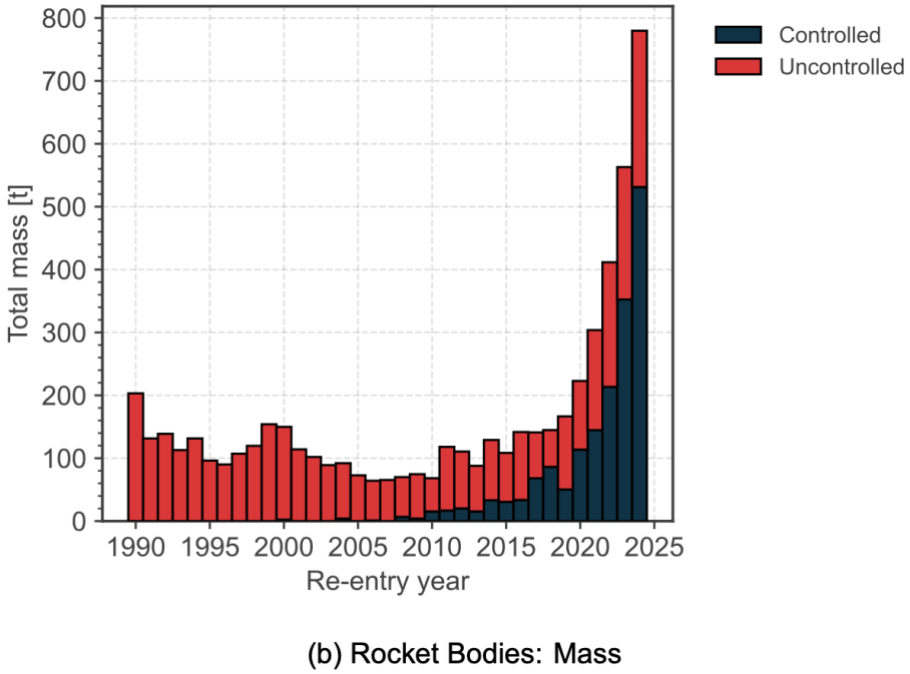

figure 6. controlled and uncontrolled re-entries for Rocket Bodies (credit: ESA)

The exponential growth in the number of objects in orbit poses global risks, as accidental collisions – made more likely by the increasing number of satellites travelling along orbits at the same altitude – generate an indefinite quantity of debris. Regardless of their size, these fragments act as weapons, damaging other satellites and triggering an inexorable chain reaction.

In addition to rendering satellites inoperable, this scenario presents an ever-growing risk for future human missions, which are forced to pass through these overcrowded orbital regions.

Circular economy

One of the greatest challenges of long-distance space travel and the establishment of bases beyond Earth orbit is the ability to provide food, water, and a breathable atmosphere in a stable, safe, and highly reliable manner over time.

To enable such missions, it has become necessary to develop a highly efficient system capable of recovering nutrients from waste streams, thereby minimising the need for external consumable supplies: this involves the actual recovery of valuable minerals from waste products.

The circular economy outlines systems in which the use of resources – by their nature limited – is maximised, favouring circular models among the various possible approaches.

The space sector could be considered an ideal environment in which to apply the principles of the circular economy, and what happens in space should be taken as a case study to develop ways of living that move as far as possible from the linear consumption model to which we are accustomed.

> The circular economy is a model of production and consumption that involves sharing, leasing, reusing, repairing, refurbishing, and recycling existing materials and products for as long as possible.

The words of Antonio Massarutto are particularly resonant in this context:

> Every vital process produces waste. But there is a difference between producing waste and producing rubbish.

The European Space Agency (ESA) has actively supported this cause, working to develop new systems capable of resupplying and servicing satellites in orbit, thereby extending their operational lifespan and reducing their environmental impact.

The hope is to eventually be able to assemble, manufacture, and recycle directly in orbit.

Removal techniques

There are several possible approaches to mitigate the creation of new debris and to clean up the space environment.

First of all, the number of new launches could be reduced, thus limiting the introduction of additional objects into space. Satellites could be made more resistant, or measures could be taken to shorten their time in orbit. Residual energy sources can also be eliminated to prevent the risk of explosions, or shielding can be added to prevent fragmentation.

Unfortunately, only about half of end-of-life satellites currently comply with these measures, whereas achieving tangible results would require much higher levels of adherence – around 90%.

Traditional satellites, burning up upon atmospheric re-entry, release aluminium particles and other metals that can persist for decades in the thermosphere, with effects on the

climate and ozone layer that are still poorly studied. The idea, therefore, was to construct a wooden satellite because this material burns up completely without releasing harmful residues, reducing orbital pollution. [21]

In 2018, ClearSpace was founded out of the awareness that in-orbit servicing and the removal of space debris are essential services for the future of space exploration and operations. [17]

Satellites of the future will increasingly need to be designed with their removal in mind. For example, the company Astroscale has developed a docking plate – a device to be installed on the satellite before launch, helping to reduce development costs and enabling the satellite to be captured at the end of its life. Through its Cosmic mission, the company is also implementing a new capture technology using a robotic arm. [22]

Further information can be found at [16] and [19].

Third Chapter

Trajectory optimization

Why discuss optimal control?

When controlling a dynamic system – such as a rocket following an ascent trajectory or a rover performing tasks – the goal is to operate the system in the best possible way. This might involve, for instance, minimising energy consumption or reaching a destination in the shortest time possible.

This, in essence, is the crux of optimal control: finding the control strategy that optimises system performance while adhering to any constraints.

The first essential step is describing the system to be controlled. One must understand how it behaves over time, and to do so, a mathematical model is required – one that represents the relationship between the system's current state and the control decisions being made.

The system's state changes based on control actions; without a model describing this relationship, it becomes impossible to predict how these actions will influence the system, rendering optimisation unattainable. The mathematical model thus provides the foundation for all subsequent reasoning.

Optimal control problem

Control systems are described by ordinary differential equations (ODEs) of the form:

$$\dot{x} = f(t, x, u), \quad x(t_0) = x_0 \tag{1}$$

where:

- x is the state vector ($x \in \mathbb{R}^n$),
- u is the control input, taking values from the admissible set $\mathcal{U} \in \mathbb{R}^m$,
- t denotes time,
- t_0 is the initial time and x_0 the initial state.

Both x and u are functions of time t.

Once the system's dynamics are understood, the key question arises: what should be optimised?

This is where the cost function (or objective function) comes into play – it translates the goal into a mathematical form. Without a well-defined cost function, it would be impossible to compare control solutions or measure how close a strategy is to optimality. The cost function penalises undesirable behaviours, such as deviations from the desired state or excessive resource usage.

For a given initial condition (t_0, x_0), system behaviours are parametrised by control functions u. Thus, a cost functional $\mathcal{J}$ assigns a value to each admissible control:

$$\mathcal{J}(u) = \varphi\left(\vec{x}_0, \vec{x}_f, t_0, t_f\right) + \int_{t_0}^{t_f} [\Phi(x(t), u(t), t)]dt \tag{2}$$

where:

- Φ is the running cost (quantifying trajectory performance),
- φ is the terminal cost (quantifying final-state achievement),
- t_f is the final time (free or fixed),
- $x_f = x\left(t_f\right)$ is the final state (free, fixed, or from a target set).

For brevity, we write $\mathcal{J}(u)$, though $\mathcal{J}$ technically depends on initial/final conditions and u: $\mathcal{J}\left(\vec{x}_0, \vec{x}_f, t_0, t_f, u\right)$.

The equation (2) can be rewritten in the Lagrange or Mayer formulations by nullifying φ or Φ, respectively, and introducing suitable auxiliary variables.

The optimal control problem reduces to: find the control u that minimises $\mathcal{J}(u)$ among all admissible controls (or at least locally).

However, constraints must be introduced to ensure physical feasibility. Ignoring them risks yielding a theoretically optimal but practically unrealisable solution. Boundary conditions t_0 and t_f define a Two-Point Boundary Value Problem (TPBVP), which may include initial/terminal conditions: $\vec{x}(t_0) = \vec{x}_0$, $\vec{x}\left(t_f\right) = \vec{x}_f$.

The constraint vector is:

$$\vec{\chi}\left(\vec{x}_0, \vec{x}_f, t_0, t_f\right) = \vec{0} \tag{3}$$

where $\vec{\chi}$: $[\mathbb{R}^n, \mathbb{R}^n, \mathbb{R}, \mathbb{R}] \to \mathbb{R}^q$.

This general framework is termed the Bolza problem, solvable via analytical, numerical, or hybrid methods.

Necessary Conditions for Optimality

A first-order necessary condition for constrained optimality requires the first variation of $\mathcal{J}$ to vanish for all admissible trajectory perturbations. To apply indirect methods, we reformulate (2) using Lagrange multipliers μ (for boundary constraints) and adjoint variables λ (for state dynamics):

$$\mathcal{J}^* = \varphi + \vec{\mu}^T\vec{\chi} + \int_{t_0}^{t_f}\left[\Phi + \vec{\lambda}^T\left(\vec{f} - \dot{\vec{x}}\right)\right]dt \tag{4}$$

The Lagrange multipliers are constants associated with the boundary conditions (BCs), providing a measure of how well the constraints are satisfied.

The adjoint variables (also called costates), linked to the state variables, represent the influence of each state variable on the performance index.

The augmented functional $\mathcal{J}^*$ coincides with $\mathcal{J}$ when $\vec{\chi} = 0$ and $\left(\vec{f} - \dot{\vec{x}}\right) = 0$.

By manipulating the previous equation (4), we may simplify it through integration by parts to eliminate the state derivatives $\dot{\vec{x}}$:

$$\int_{t_0}^{t_f}\left(\vec{\lambda}^T\dot{\vec{x}}\right)dt = \left(-\vec{\lambda}_f^T\dot{\vec{x}}_f\right) + \left(\vec{\lambda}_0^T\dot{\vec{x}}_0\right) + \int_{t_0}^{t_f}\left(\dot{\vec{\lambda}}^T\vec{x}\right)dt$$

The augmented functional thus becomes:

$$\mathcal{J}^* = \varphi + \vec{\mu}^T\vec{\chi} + \left(\vec{\lambda}_0^T\dot{\vec{x}}_0 - \vec{\lambda}_f^T\dot{\vec{x}}_f\right) + \int_{t_0}^{t_f}\left(\Phi + \vec{\lambda}^T\vec{f} + \dot{\vec{\lambda}}^T\vec{x}\right)dt$$

We may consolidate the integrand by introducing the fundamental Hamiltonian function:

$$\mathcal{H} \triangleq \Phi + \vec{\lambda}^T\vec{f} \tag{5}$$

Examining the first variation of $\mathcal{J}$ yields:

$$\begin{aligned}\delta\mathcal{J}^* = &\left(\frac{\partial\varphi}{\partial t_0} + \vec{\mu}^T\frac{\partial\vec{\chi}}{\partial t_0} - \mathcal{H}_0\right)\delta t_0 + \\ &+\left(\frac{\partial\varphi}{\partial t_f} + \vec{\mu}^T\frac{\partial\vec{\chi}}{\partial t_f} + \mathcal{H}_f\right)\delta t_f + \\ &+\left(\frac{\partial\varphi}{\partial\vec{x}_0} + \vec{\mu}^T\frac{\partial\vec{\chi}}{\partial\vec{x}_0} + \vec{\lambda}_0^T\right)\delta\vec{x}_0 + \\ &+\left(\frac{\partial\varphi}{\partial\vec{x}_f} + \vec{\mu}^T\frac{\partial\vec{\chi}}{\partial\vec{x}_f} - \vec{\lambda}_f^T\right)\delta\vec{x}_f +\end{aligned} \tag{6}$$

$$+\int_{t_0}^{t_f}\left[\left(\frac{\partial\mathcal{H}}{\partial\vec{x}}+\dot{\vec{\lambda}}^T\right)\delta\vec{x}+\frac{\partial\mathcal{H}}{\partial\vec{u}}\delta\vec{u}\right]dt$$

The functional $\mathcal{J}$ (2) attains its maximum when $\delta\mathcal{J}^* \leq 0\ \forall d\vec{x}$.

To achieve this, one must define an appropriate set of Lagrange multipliers and adjoint variables. For the functional's first variation to vanish, the coefficients of the parenthetical terms must be nullified:

$$\frac{\partial\varphi}{\partial t_0}+\vec{\mu}^T\frac{\partial\vec{\chi}}{\partial t_0}-\mathcal{H}_0=0 \quad\rightarrow\quad \mathcal{H}_0=\frac{\partial\varphi}{\partial t_0}+\vec{\mu}^T\frac{\partial\vec{\chi}}{\partial t_0}$$

$$\frac{\partial\varphi}{\partial t_f}+\vec{\mu}^T\frac{\partial\vec{\chi}}{\partial t_f}+\mathcal{H}_f=0 \quad\rightarrow\quad \mathcal{H}_f=-\frac{\partial\varphi}{\partial t_f}-\vec{\mu}^T\frac{\partial\vec{\chi}}{\partial t_f}$$

$$\frac{\partial\varphi}{\partial\vec{x}_0}+\vec{\mu}^T\frac{\partial\vec{\chi}}{\partial\vec{x}_0}+\vec{\lambda}_0^T=0 \quad\rightarrow\quad \vec{\lambda}_0^T=-\frac{\partial\varphi}{\partial\vec{x}_0}-\vec{\mu}^T\frac{\partial\vec{\chi}}{\partial\vec{x}_0}$$

$$\frac{\partial\varphi}{\partial\vec{x}_f}+\vec{\mu}^T\frac{\partial\vec{\chi}}{\partial\vec{x}_f}-\vec{\lambda}_f^T=0 \quad\rightarrow\quad \vec{\lambda}_f^T=\frac{\partial\varphi}{\partial\vec{x}_f}+\vec{\mu}^T\frac{\partial\vec{\chi}}{\partial\vec{x}_f}$$

These yield the transversality conditions (time-governing ODEs) and optimality conditions (state-governing ODEs) at the trajectory boundaries (TPBVP). The final time t_f and final state x_f may be either free, fixed, or constrained to a target set.

Key Observations:

- fixed time $(t \in \vec{\chi})$:

  time derivatives vanish $\frac{\partial\vec{\chi}}{\partial t_0},\frac{\partial\vec{\chi}}{\partial t_f}=0$. The Hamiltonian becomes free and subject to optimisation.

- free time $t \notin \vec{\chi}$:

  when $\varphi = m$ (independent of time), the Hamiltonian vanishes and time becomes an optimisation variable.

- constrained state $x_i \in \vec{\chi}$:

  state derivatives vanish, leaving the corresponding adjoint variable free for optimisation.

- free state $x_i \notin \vec{\chi}$:

  if $\varphi = m$ (independent of x_i), the adjoint variable becomes null.

Euler-Lagrange Equations and Control Law

The remaining terms in the variation (6) yield:

$$\int_{t_0}^{t_f} \left[\left(\frac{\partial \mathcal{H}}{\partial \vec{x}} + \dot{\vec{\lambda}}^T \right) \delta \vec{x} + \frac{\partial \mathcal{H}}{\partial \vec{u}} \delta \vec{u} \right] dt$$

Nullifying $\delta \vec{x}$ gives the Euler-Lagrange equations for adjoints:

$$\frac{\partial \vec{\lambda}}{\partial t} = -\left(\frac{\partial \mathcal{H}}{\partial x} \right)^T \tag{7}$$

Nullifying $\delta \vec{u}$ produces m algebraic equations:

$$\left(\frac{\partial \mathcal{H}}{\partial \vec{u}} \right)^T = \vec{0} \tag{8}$$

The input control $u \in \mathcal{U} \subseteq \mathbb{R}^m$ is constrained within bounds $\mathcal{U}_{\min} \leq u \leq \mathcal{U}_{MAX}$.

Pontryagin's Maximum Principle (PMP)

These considerations – specifically that the control u must maximise (or minimise) the Hamiltonian with respect to itself – constitute Pontryagin's Maximum Principle. The optimal control value u^* must, at every point along the trajectory, maximise the Hamiltonian to ensure the functional $\mathcal{J}$ is maximised.

Therefore:

- when the control is bounded within an admissible set $\mathcal{U}$, the optimal control law is determined by (7);
- for unbounded controls, the optimal value must coincide with either extremum of $\mathcal{U}$ (maximum or minimum).

The solution of these equations fundamentally depends on the functional relationship between the Hamiltonian and control vector: when this relationship is linear, the condition (8) becomes unsolvable, rendering the control mathematically indeterminate. For a control-affine Hamiltonian where:

$$\frac{\partial \mathcal{H}}{\partial u} = k_{u_i} \quad \left(k_{u_i} = constant \right)$$

Pontryagin's Maximum Principle (PMP) requires:

$$u_i^* = \begin{cases} \mathcal{U}_{min} \; if \; k_{u_i} < 0 \\ \mathcal{U}_{MAX} \; if \; k_{u_i} > 0 \end{cases}$$

This discontinuous switching behaviour characterises bang-bang control.

To enhance code robustness and mitigate discontinuities in trajectory variables (which may arise from local constraints during transfer), we implement a temporal domain decomposition strategy. The integration interval is partitioned into n_p subintervals (arcs), with discontinuities and constraints explicitly positioned at arc boundaries.

Numerical Implementation:

- arc partitioning

  The trajectory is divided into n_p arcs, creating (n_p) junction points. The j-th arc spans $t_{(j-1)+}$ to $t_{(j)-}$, with state variables transitioning from $\vec{x}_{(j-1)+}$ to $\vec{x}_{(j)+}$ $(j = 1, \dots, f)$.

- Multi-Point Boundary Value Problem (MPBVP) Formulation:

$$\vec{\chi}\left(\vec{x}_{(j-1)+}, \vec{x}_{(j)+}, t_{(j-1)+}, t_{(j)-}\right) = \vec{0}, \quad j = 1, \dots, n_p$$

- cost functional:

$$\mathcal{J} = \varphi\left(\vec{x}_0, \vec{x}_{1\pm}, \dots, \vec{x}_f, t_0, t_{1\pm}, \dots, t_f\right) + \sum_{j=1}^{n_p} \int_{t_{(j-1)+}}^{t_{(j)-}} \left[\vec{\Phi}(\vec{x}(t), \vec{u}(t), t)\right] dt$$

  and the augmented cost functional:

$$\mathcal{J}^* = \varphi + \vec{\mu}^T \vec{\chi} + \sum_{j=1}^{n_p} \int_{t_{(j-1)+}}^{t_{(j)-}} \left[\vec{\lambda}^T \left(\vec{f} - \dot{\vec{x}}\right)\right] dt$$

Through integration by parts, we derive the augmented functional:

$$\mathcal{J}^* = \varphi + \vec{\mu}^T \vec{\chi} + \sum_{j=1}^{n_p} \left(\vec{\lambda}^T_{(j-1)+} \vec{x}_{(j-1)+} - \vec{\lambda}^T_{(j)-} \vec{x}_{(j)-}\right) + \sum_{j=1}^{n_p} \int_{t_{(j-1)+}}^{t_{(j)-}} \left(\vec{\lambda}^T \vec{f} + \dot{\vec{\lambda}}^T \vec{x}\right) dt$$

Differential Form:

$$\begin{aligned}
\delta\mathcal{J}^* = &\left(\frac{\partial \vec{\varphi}}{\partial t_{(j-1)+}} + \vec{\mu}^T \frac{\partial \vec{\chi}}{\partial t_{(j-1)+}} - \mathcal{H}_{(j-1)+}\right) \delta t_{(j-1)+} + \\
&+ \left(\frac{\partial \vec{\varphi}}{\partial t_{(j)-}} + \vec{\mu}^T \frac{\partial \vec{\chi}}{\partial t_{(j)-}} + \mathcal{H}_{(j)-}\right) \delta t_{(j)-} + \\
&+ \left(\frac{\partial \vec{\varphi}}{\partial \vec{x}_{(j-1)+}} + \vec{\mu}^T \frac{\partial \vec{\chi}}{\partial \vec{x}_{(j-1)+}} + \vec{\lambda}^T{}_{(j-1)+}\right) \delta \vec{x}_{(j-1)+} + \\
&+ \left(\frac{\partial \vec{\varphi}}{\partial \vec{x}_{(j)-}} + \vec{\mu}^T \frac{\partial \vec{\chi}}{\partial \vec{x}_{(j)-}} - \vec{\lambda}^T{}_{(j)-}\right) \delta \vec{x}_{(j)-} +
\end{aligned}$$

$$+\sum_{j=1}^{n_p}\int_{t_{(j-1)+}}^{t_{(j)-}}\left[\left(\frac{\partial\mathcal{H}}{\partial\vec{x}}+\dot{\vec{\lambda}}^T\right)\delta\vec{x}+\frac{\partial\mathcal{H}}{\partial\vec{u}}\delta\vec{u}\right]dt$$

The transversality and optimality conditions at generic junction point j become:

$$\frac{\partial\vec{\varphi}}{\partial t_{j+}}+\vec{\mu}^T\frac{\partial\vec{\chi}}{\partial t_{j+}}-\mathcal{H}_{j+}=0,\quad j=1,\dots,n_p-1$$

$$\frac{\partial\vec{\varphi}}{\partial t_{j-}}+\vec{\mu}^T\frac{\partial\vec{\chi}}{\partial t_{j-}}+\mathcal{H}_{j-}=0,\quad j=1,\dots,n_p$$

$$\frac{\partial\vec{\varphi}}{\partial\vec{x}_{j+}}+\vec{\mu}^T\frac{\partial\vec{\chi}}{\partial\vec{x}_{j+}}+\vec{\lambda}^T{}_{j+}=0,\quad j=1,\dots,n_p-1$$

$$\frac{\partial\vec{\varphi}}{\partial\vec{x}_{j-}}+\vec{\mu}^T\frac{\partial\vec{\chi}}{\partial\vec{x}_{j-}}-\vec{\lambda}^T{}_{j-}=0,\quad 1,\dots,n_p$$

For further details and explanations, please refer to: [2], [7].

Numerical methods

A numerical method is a mathematical strategy employed to solve problems that prove challenging to address through precise analytical techniques, typically due to the complexity of the governing equations. The core objective is to decompose a complex problem into a series of smaller, more manageable sub-problems.

The fundamental concept involves transforming sets of differential equations – which represent continuous phenomena in time or space – into discrete systems comprising a finite number of points (intervals) defined by a reduced set of variables. While the trajectory optimization problem under consideration is inherently continuous in time, numerical methods enable its reformulation from an infinite-dimensional problem into a series of finite-dimensional sub-problems.

Given the inherent difficulty in solving Boundary Value Problems (BVPs) analytically, numerical methods are frequently employed to approximate solutions. Common techniques include:

- *Shooting Method*

  The shooting method converts a BVP into an initial value problem by:

  - proposing trial initial conditions
  - forward-integrating the differential equations

  - iteratively adjusting initial guesses until terminal conditions are satisfied

  Advantages: effective for both linear and nonlinear problems

  Limitations: potential instability for stiff systems and reduced efficacy for highly sensitive problems

- *Finite Difference Method*

  This approach:

  - discretizes the time domain into a grid
  - approximates derivatives using finite differences
  - transforms the continuous problem into a solvable algebraic system

- *Collocation Methods*

  These methods:

  - employ basis functions to approximate solutions
  - reformulate the problem as a function approximation task
  - particularly suited to nonlinear problems

- *Newton/Extended Newton-Raphson Method*

  For nonlinear systems, this technique:

  - linearizes equations via Taylor expansions
  - iterates to convergence
  - offers enhanced efficacy for complex nonlinearities

The Single Shooting Method is particularly useful when dealing with ODEs or systems of differential equations, where the initial or final conditions are not completely known and must be determined as part of the solution.

The main approach is to reduce the boundary value problem to an Initial Value Problem (IVP); this is done through an iterative technique:

1. initial values are hypothesized for the unknown variables;
2. the system of differential equations is solved with these initial conditions; for example, using standard methods for solving IVPs, such as Runge-Kutta or Euler methods;

3. the solution obtained at the end of the interval is compared with the known final conditions. If the solution does not satisfy the final conditions (i.e., there is an error), optimization or correction techniques are used, for example Newton methods, to adjust the initial values and repeat the process until the error is sufficiently small.

It works well when the problem is not too stiff or highly nonlinear.

The method can be unstable for some problems, especially when the solution is very sensitive to initial conditions.

It is not suitable for problems with many unknown parameters or very complex systems, where methods such as Multiple Shooting or collocation methods are preferable.

Returning to the work of this thesis, it was chosen to implement a shooting procedure with bang-bang control by evaluating, at each iteration, the discrepancy between the obtained result $x_j(t_f)$ and the desired state x_f.

This result is then used to correct the initial hypothesis, thus obtaining a new trial value that will be used in the next iteration, and so on until the predetermined error threshold is reached.

If we consider the vector containing the initial hypotheses:

$$\vec{x}_0 = \{x_1, x_2, \dots, x_n\}^T$$

and the vector of the final values we want to achieve:

$$\vec{x}_f^* = \{x_1^*, x_2^*, \dots, x_n^*\}^T$$

Then, the discrepancy can be calculated as:

$$\vec{\chi}(\vec{x}_f^*) = \begin{cases} \chi_1 \\ \chi_2 \\ \dots \\ \chi_n \end{cases} = \begin{cases} x_1 - x_1^* \\ x_2 - x_2^* \\ \dots \\ x_n - x_n^* \end{cases}$$

In this way, the entire process is repeated, iteration by iteration, until the optimal initial guess is found that guarantees $\vec{\chi}(\vec{x}_f^*) = \vec{0}$.

To find this, it is necessary to apply the first-order Taylor expansion to the constraint vector:

$$\chi(x) = \chi(x_0) + \frac{\partial \chi(x_0)}{\partial x}(x - x_0)$$

In this case, the partial derivatives are calculated using the finite difference method (backward, centred, or forward in time) using the assigned initial values and perturbed values obtained by adding a constant to the initial state:

$$\tilde{x}_0 = x_0 + \delta$$

Assuming $\delta = 10^{-6}$, we construct the Jacobian matrix by perturbing each state one at a time $\left(\vec{\delta} = \delta\{1, 0, 0, \dots, 0\}^T\right)$:

$$\frac{\partial \chi(\tilde{x}_0)}{\partial \tilde{x}} = \tilde{J}(\chi(\tilde{x}_0), \tilde{x}) = \begin{bmatrix} \frac{\partial \chi_1}{\partial \tilde{x}_1} & \frac{\partial \chi_1}{\partial \tilde{x}_2} & \cdots & \frac{\partial \chi_1}{\partial \tilde{x}_n} \\ \frac{\partial \chi_2}{\partial \tilde{x}_1} & \frac{\partial \chi_2}{\partial \tilde{x}_2} & \cdots & \frac{\partial \chi_2}{\partial \tilde{x}_n} \\ \vdots & \vdots & \ddots & \vdots \\ \frac{\partial \chi_m}{\partial \tilde{x}_1} & \frac{\partial \chi_m}{\partial \tilde{x}_2} & \cdots & \frac{\partial \chi_m}{\partial \tilde{x}_n} \end{bmatrix} \tag{9}$$

Each term is calculated using the finite difference method:

$$\frac{\partial \chi}{\partial \tilde{x}_j^*} = \frac{\chi - \chi^*}{\delta}$$

and the matrix $\tilde{J} \in \mathbb{R}^{m \times n}$, where m is the number of constrained quantities in the vector χ and n is the number of state variables.

Applying this procedure at each iteration, we can find the initial state hypothesis to use in the next iteration as a correction of the previous one, following:

$$\chi(\tilde{x}_{j+1}) = \chi(\tilde{x}_j) + \frac{\partial \chi(\tilde{x}_j)}{\partial \tilde{x}_{j+1}}(\tilde{x}_{j+1} - \tilde{x}_j)$$

It is possible to derive the new initial state hypothesis. Assuming that the solution found at iteration $(j+1)$ exists, we obtain: $\chi(\tilde{x}_j) + \tilde{J}(\tilde{x}_{j+1} - \tilde{x}_j) = 0$. Therefore, we have:

$$\tilde{x}_{j+1} = \tilde{x}_j - \left[\tilde{J}(\chi_j)\right]^{-1} \chi(\tilde{x}_j)$$

Fourth Chapter

Dynamic model

n-body problem

The n-body problem (nBP) consists of predicting and studying the motion of a system of n celestial bodies interacting with each other. Let us consider n bodies in an isolated system with comparable masses – for example, the various planets of the Solar System. We choose an inertial reference frame, that is, a reference frame at rest or in uniform rectilinear motion relative to the fixed stars (if the system were not inertial, we would need to add non-inertial contributions to the force scheme, such as fictitious forces like the Coriolis force and centripetal force).

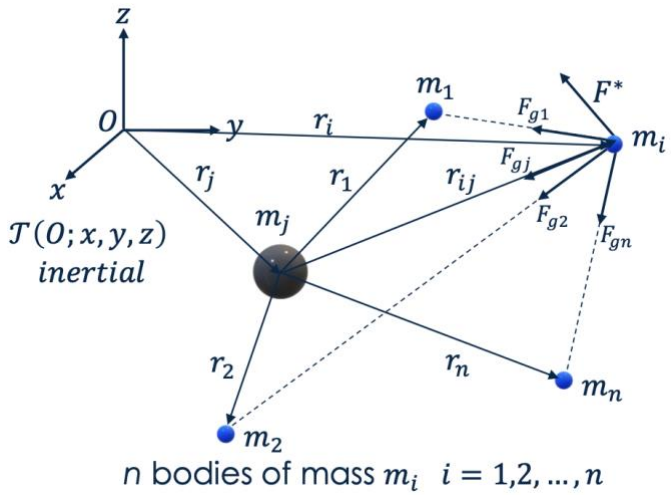

figure 7. n-body system (credit: lessons on orbital mechanics)

On each body act:

- the gravitational contributions from all other bodies
- an additional force $\vec{F}^*$ accounting for all other possible contributions due to:
    - non-sphericity of the body
    - thrust generated if the body is a spacecraft
    - aerodynamic drag
    - solar pressure
    - other effects

From this scheme, we derive the following vector relation:

$$\vec{r}_{ij} = \vec{r}_i - \vec{r}_j$$

Expressing the gravitational contribution according to Newton's law and applying the second law of dynamics, we obtain:

$$\vec{F} = \vec{F}^* + \sum_{j=1, j\neq i}^{n} \overrightarrow{F_g}_j = \vec{F}^* - Gm_i \sum_{j=1, j\neq i}^{n} \frac{m_j}{r_{ij}^3} \vec{r}_{ij}$$

Since:

$$\vec{F} = \frac{d}{dt}(m\vec{v}_i) \;\rightarrow\; -Gm_i \sum_{j=1, j\neq i}^{n} \frac{m_j}{r_{ij}^3} \vec{r}_{ij} = m_i \ddot{\vec{r}}_i$$

Therefore:

$$\ddot{\vec{r}}_i = -\sum_{j=1, j\neq i}^{n} \frac{Gm_j}{r_{ij}^3} \vec{r}_{ij} = -\sum_{j=1, j\neq i}^{n} \frac{\mu_j}{r_{ij}^3} \vec{r}_{ij}$$

Solving this equation means solving the nBP. In reality, this is a system of n coupled second-order vector differential equations (i.e., each single equation contains multiple unknowns), thus requiring a numerical solver for simultaneous solution.

Once the unknowns (accelerations) are determined, they must be integrated twice to obtain the r_i, representing the relative positions of the bodies as functions of time.

The solution provided by the solver is called orbital propagation, to which perturbative errors must be added for a more accurate solution.

Two-body problem

The nBP can be simplified to the two-body case, whose main advantage is the possibility of using an analytical approach rather than numerical solvers.

The fundamental assumptions of this problem are:

- the system consists of only two masses m_1 and m_2 with $m_1 \gg m_2$ [e.g., Earth-Moon (EM) or Earth-Sun (SE) systems]
- no external forces act on the bodies ($\vec{F}^* = \vec{0}$ – only gravitational forces along the line connecting their centres)
- perfect spherical symmetry (mass concentrated at the centre of mass)
- constant masses $\left(\frac{dm_1}{dt} = 0, \frac{dm_2}{dt} = 0\right)$

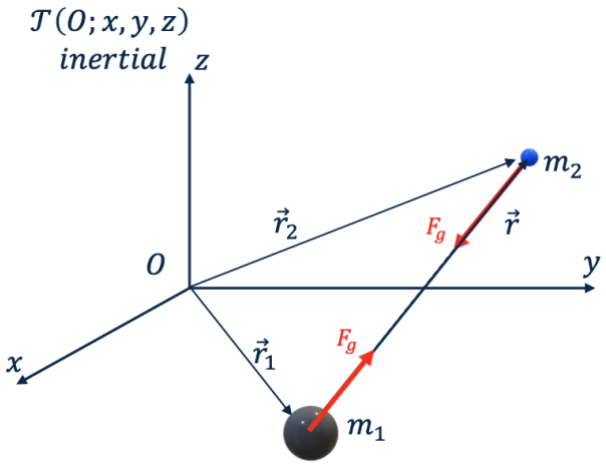

figure 8. 2-body scheme (credit: lessons on orbital mechanics)

Mathematical Formulation

We define the relative position vector:

$$\vec{r} = \vec{r}_2 - \vec{r}_1$$

Its derivatives give relative velocity and acceleration:

$$\dot{\vec{r}} = \dot{\vec{r}}_2 - \dot{\vec{r}}_1$$

$$\ddot{\vec{r}} = \ddot{\vec{r}}_2 - \ddot{\vec{r}}_1$$

By writing Newton's law of universal gravitation for both bodies and combining them, we can derive the equation governing the motion of the two-body system:

$$\begin{cases} m_2\ddot{\vec{r}}_2 = -G\dfrac{m_1 m_2}{r^3}\vec{r} \;\; (I) \\ m_1\ddot{\vec{r}}_1 = G\dfrac{m_1 m_2}{r^3}\vec{r} \;\; (II) \end{cases}$$

Subtracting (I) from (II):

$$(II)-(I): \quad \ddot{\vec{r}}_2 - \ddot{\vec{r}}_1 = \ddot{\vec{r}} = -G\frac{m_1}{r^3}\vec{r} - G\frac{m_2}{r^3}\vec{r} = -G(m_1+m_2)\frac{\vec{r}}{r^3}$$

For $m_1 = M$ (primary body) and $m_2 = m$ (secondary body), with $\mu = GM$ (gravitational parameter), and since $M + m \simeq M \;\rightarrow\; G(M+m) \simeq GM = \mu$:

$$\ddot{\vec{r}} = -G\frac{(M+m)}{r^3}\vec{r} \;\rightarrow\; \ddot{\vec{r}} + \frac{\mu}{r^3}\vec{r} = \vec{0} \qquad (10)$$

The resulting equation demonstrates that the acceleration of both bodies is purely radial, which is entirely consistent with the assumption that gravity is the sole force acting on them.

This two-body equation is fundamentally a dynamical equation because the gravitational parameter μ inherently contains mass information.

The gravitational field is conservative – the work done by gravitational forces between any two points A and B in space depends solely on their initial and final positions, not on the path taken. This property allows us to define a gravitational potential and confirms that mechanical energy (the sum of kinetic and potential energy) is conserved. Energy can only be converted between these two forms:

$$Mechanical\ Energy\ =\ Kinetic\ Energy\ +\ Potential\ Energy$$

In its general formulation:

$$\mathcal{E} = \frac{v^2}{2} - \frac{\mu}{r} = c \implies \mathcal{E} = \frac{v^2}{2} + \left(c - \frac{\mu}{r}\right) \tag{11}$$

Here, c is an arbitrary constant whose value depends on the zero potential energy reference. Specifically:

- $c = 0$ corresponds to setting the potential energy reference at infinity
- The satellite's potential energy $\left(-\frac{\mu}{r}\right)$ is consequently always negative

Specific Mechanical Energy $\mathcal{E}$:

For a satellite, this parameter represents the sum of its kinetic energy per unit mass and potential energy per unit mass. It remains constant throughout the orbit, neither increasing nor decreasing due to the satellite's motion.

Angular Momentum Conservation:

Beginning with the two-body equation:

$$\ddot{\vec{r}} = -\frac{\mu}{r^3}\vec{r}$$

Taking the cross product with $\vec{r}$:

$$\vec{r} \times \ddot{\vec{r}} = -\vec{r} \times \frac{\mu}{r^3}\vec{r} = -\frac{\mu}{r^3}(\vec{r} \times \vec{r}) = 0$$

From the definition of angular momentum:

$$\vec{h} \triangleq \vec{r} \times \vec{v} = \vec{r} \times \dot{\vec{r}} \tag{12}$$

The time derivative of angular momentum is zero, proving its conservation:

$$\frac{d}{dt}(\vec{r}\times\dot{\vec{r}}) = \dot{\vec{r}}\times\dot{\vec{r}} + \vec{r}\times\ddot{\vec{r}} = 0 \;\Rightarrow\; \vec{r}\times\dot{\vec{r}} = \vec{r}\times\vec{v} = constant$$

$\vec{h}\perp(\vec{r}\times\vec{v}) \implies \vec{h}$ is always perpendicular to the plane containing $\vec{r}$ and $\vec{v}$

Reformulating the Two-Body Equation

Starting again with:

$$\ddot{\vec{r}} = -\frac{\mu}{r^3}\vec{r}$$

Taking the cross product with $\vec{h}$:

$$\ddot{\vec{r}}\times\vec{h} = \frac{\mu}{r^3}(\vec{h}\times\vec{r})$$

The left-hand side can be rewritten as:

$$\ddot{\vec{r}}\times\vec{h} = \frac{d}{dt}(\dot{\vec{r}}\times\vec{h})$$

The right-hand side becomes:

$$\frac{\mu}{r^3}(\vec{h}\times\vec{r}) = \frac{\mu}{r^3}\left[(\vec{r}\times\dot{\vec{r}})\times\vec{r}\right] = \frac{\mu}{r^3}\left[(\vec{r}\cdot\vec{r})\dot{\vec{r}} - (\vec{r}\cdot\dot{\vec{r}})\vec{r}\right] =$$

$$= \frac{\mu}{r^3}\left(r^2\dot{\vec{r}} - r\dot{r}\vec{r}\right) = \frac{\mu}{r}\dot{\vec{r}} - \frac{\mu}{r^2}\dot{r}\vec{r}$$

Noting that: $\frac{\mu}{r}\dot{\vec{r}} - \frac{\mu}{r^2}\dot{r}\vec{r} = \mu\frac{d}{dt}\left(\frac{\vec{r}}{r}\right)$

Combining both sides:

$$\frac{d}{dt}(\dot{\vec{r}}\times\vec{h}) = \mu\frac{d}{dt}\left(\frac{\vec{r}}{r}\right)$$

Integrating yields:

$$\dot{\vec{r}}\times\vec{h} = \mu\left(\frac{\vec{r}}{r}\right) + \vec{B}$$

where $\vec{B}$ is an integration constant.

Taking the dot product with $\vec{r}$:

$$\vec{r}\cdot\dot{\vec{r}}\times\vec{h} = \vec{r}\cdot\mu\left(\frac{\vec{r}}{r}\right) + \vec{r}\cdot\vec{B}$$

The left-hand side (LHS) simplifies to: $\vec{r}\cdot\dot{\vec{r}}\times\vec{h} = \vec{r}\times\dot{\vec{r}}\cdot\vec{h} = \vec{h}\cdot\vec{h} = h^2$

The right-hand side (RHS) becomes: $\vec{r}\cdot\mu\left(\frac{\vec{r}}{r}\right) + \vec{r}\cdot\vec{B} = \mu\left(\frac{r^2}{r}\right) + rB\cos\nu$

where ν is the angle between $\vec{B}$ and $\vec{r}$.

Solving for r gives the polar equation of the orbit:

$$r = \frac{\frac{h^2}{\mu}}{1 + \left(\frac{B}{\mu}\right)\cos\nu} \tag{13}$$

This represents the fundamental orbital equation in terms of angular momentum and integration constants.

Equation of the orbit

To identify the trajectory represented by the fundamental orbital equation, we can compare the polar trajectory equation (13) with the general equation of a conic section:

$$r = \frac{p}{1 + e\cos\nu} \tag{14}$$

where:

- ν, the true anomaly, represents the time-dependent polar angle between vectors $\vec{B}$ and $\vec{r}$, or equivalently, the angle between $\vec{r}$ and the conic's closest point to the focus (periapsis)
- p is the semi-latus rectum (a geometric constant of the orbit)
- e is the eccentricity, determining the conic section type

This mathematical equivalence validates Kepler's First Law while extending it to all conic sections and establishes that:

- conic sections are the only possible two-body problem solutions
- the orbital focus coincides with the central body's centre of mass
- specific mechanical energy ($\mathcal{E}$) remains constant
- specific angular momentum (h) is conserved
- the orbital plane is fixed in inertial space

In our solar system, Earth and Venus exhibit nearly circular orbits ($e \approx 0$) but most celestial bodies follow elliptical orbits ($0 < e < 1$). All orbiting bodies rotate around a common barycentre.

Key Relationships

Semi-latus Rectum:

$$p = \frac{h^2}{\mu}$$

shows the direct dependence on the satellite's specific angular momentum.

Energy Equation (specialized for periapsis):

$$\mathcal{E} = \frac{v^2}{2} - \frac{\mu}{r} = \frac{h^2}{2r_p^2} - \frac{\mu}{r_p}$$

where: $\begin{cases} r_p = a(1-e) \\ h^2 = p\mu = \mu a(1-e^2) \end{cases}$

so:

$$\mathcal{E} = \frac{\mu a(1-e^2)}{2a^2(1-e)^2} - \frac{\mu}{a(1-e)} = -\frac{\mu}{2a} \quad (15)$$

This demonstrates that the specific mechanical energy depends solely on the orbit's semi-major axis a.

Conic Section Classification

The eccentricity e determines the orbit type:

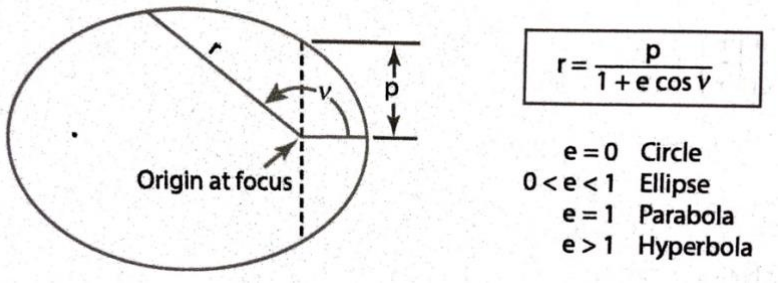

figure 9. orbit classification (credit: 6)

Characteristic velocities

Circular velocity

Represents the velocity required to maintain a satellite in a circular orbit. The satellite must be launched horizontally at the desired altitude to achieve this orbit. Using the energy equation:

$$\mathcal{E} = \frac{v^2}{2} - \frac{\mu}{a} \xrightarrow{[v = v_c \ \& \ a = r]} \frac{v_c^2}{2} - \frac{\mu}{r} = -\frac{\mu}{2r} \quad \rightarrow \quad v_c = \sqrt{\frac{\mu}{r}}$$

Note: Larger orbital radii require lower circular velocities. Elliptical orbits have variable velocity.

Escape velocity

While gravitational fields extend infinitely, their strength diminishes rapidly. The minimum velocity needed to overcome gravity and reach infinite distance is:

$$\mathcal{E} = \frac{v_e^2}{2} - \frac{\mu}{r} = \frac{v_\infty^2}{2} - \frac{\mu}{r_\infty} = 0 \quad \Longrightarrow \quad v_e = \sqrt{\frac{2\mu}{r}} = \sqrt{2} v_c$$

This parabolic trajectory allows exiting the planet's sphere of influence with zero relative velocity but maintaining Earth's orbital speed around the Sun.

Hyperbolic excess velocity

When exceeding escape velocity, a spacecraft retains residual velocity at infinity:

$$\mathcal{E} = -\frac{\mu}{2a} = \frac{v^2}{2} - \frac{\mu}{r} = \frac{v_\infty^2}{2} - \frac{\mu}{r_\infty} = 0 \quad \rightarrow \quad \frac{v_\infty^2}{2} = -\frac{\mu}{2a} \quad \Longrightarrow \quad v_\infty = \sqrt{-\frac{\mu}{a}} \quad (a < 0)$$

Expressed as the characteristic energy $v^2 - v_e^2 = v_\infty^2 \triangleq C_3$, crucial for interplanetary mission design.

Reference systems

To determine both the position and velocity of a spacecraft at a given time, it is necessary to adopt a reference system with:

- a defined coordinate set
- a time measurement system

The first requirement for orbit description is an appropriate inertial reference frame (RF). For solar orbits (planets, asteroids, comets, deep-space probes), the heliocentric-ecliptic coordinate system is typically used. For Earth satellites, the geocentric-equatorial system is more convenient.

A coordinate system requires specification of:

1. origin position
2. fundamental plane orientation
3. primary axis direction (X-axis)
4. Z-axis direction (perpendicular to the fundamental plane; Y-axis completes the right-handed triad)

Coordinate system types

- Sun-centred systems
    - heliocentric
    - barycentric
- Earth-centred systems
    - geocentric
    - topocentric
- Satellite orbit-based systems
    - perifocal
    - radial/normal
    - equinoctial
- Satellite body systems
    - attitude frame

Geocentric-Equatorial Coordinate System

origin	Earth's centre
fundamental plane	equatorial plane (defined by $\hat{\mathrm{I}}$ and $\hat{\mathrm{J}}$)
primary axes	$\hat{\mathrm{I}}$ parallel to vernal equinox direction ($\mathrm{X_e}$) $\hat{\mathrm{K}}$ perpendicular to equatorial plane (points toward Polaris) $\hat{\mathrm{J}}$ completes right-handed triad
application	Earth satellite orbital definition (Earth-Centred Inertial – ECI system)
notes	non-rotating relative to stars, except for equinox precession. Earth rotates within it

table 2. geocentric-equatorial coordinate system

The Earth-Centred Earth-Fixed (ECEF) system rotates with Earth (angular velocity $\omega_e \approx 7.292 \times 10^{-5}\, rad/s$) and aligns its primary axis with the Greenwich meridian. It requires an epoch definition (e.g., J2000).

Position representation methods

1. Cartesian coordinates: (x, y, z)
2. Right Ascension/Declination/Distance: (α, δ, r)
   - right ascension ($\alpha \in [0°, 360°]$): longitudinal angle from vernal equinox (positive eastward)
   - declination ($\delta \in [-90°, 90°]$): latitudinal angle (positive northward)
   - distance (r): magnitude from Earth's centre

   Conversion:

$$\begin{cases} x = r\cos\delta\cos\alpha \\ y = r\cos\delta\sin\alpha \\ z = r\sin\delta \end{cases}$$

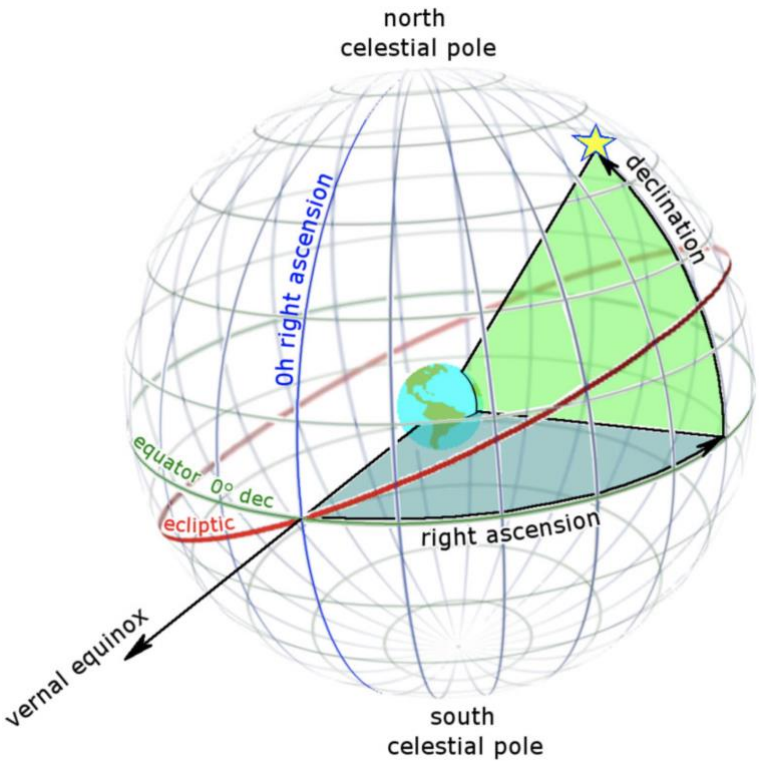

figure 10. interstellar coordination (credit: Tom Ruen / CC BY-SA 3.0)

3. Geodetic coordinates: longitude (λ), latitude (ϕ), height (h)

ZEN (Radial-Tangential-Normal) Coordinate System

origin	satellite's centre of mass
fundamental plane	equatorial plane (defined by $\hat{u}$ and $\hat{v}$ for zero inclination)
primary axes	$\hat{u}$ radial: aligned with position vector (local zenith) $\hat{v}$ tangential: eastward velocity component (along orbital path) $\hat{w}$ northward direction (orthogonal to orbital plane)
application	velocity component analysis, autonomous navigation, attitude control

table 3. ZEN coordinate system

Euler's elementary rotations

Coordinate transformations often require rotation matrices. Euler's theorem states that any rotation can be expressed as a single rotation about an axis. The elementary rotations (about $x - y - z$ axes) form a basis for all transformations:

$$R(x,\alpha) = R(\hat{\imath},\alpha) = \begin{bmatrix} 1 & 0 & 0 \\ 0 & \cos\alpha & \sin\alpha \\ 0 & -\sin\alpha & \cos\alpha \end{bmatrix} \tag{16}$$

$$R(y,\beta) = R(\hat{\jmath},\beta) = \begin{bmatrix} \cos\beta & 0 & \sin\beta \\ 0 & 1 & 0 \\ -\sin\beta & 0 & \cos\beta \end{bmatrix} \tag{17}$$

$$R(z,\gamma) = R\left(\hat{k},\alpha\right) = \begin{bmatrix} \cos\gamma & -\sin\gamma & 0 \\ \sin\gamma & \cos\gamma & 0 \\ 0 & 0 & 1 \end{bmatrix} \tag{18}$$

The key steps for composite rotations are:

1. select elementary rotation axis
2. define rotation angle
3. specify if rotation is applied to fixed or moving axes:
    - fixed axes: pre-multiply by rotation matrix
    - moving axes: post-multiply by rotation matrix

Throughout this dissertation, the predominant coordinate transformation involves conversion from the IJK inertial frame to the ZEN orbital frame, accomplished via the following Euler rotations (16), (17), (18):

- ϑ about $\hat{K}$:

$$\begin{bmatrix} \hat{I}' \\ \hat{J}' \\ \hat{K} \end{bmatrix} = R_3(\vartheta) \begin{bmatrix} \hat{I} \\ \hat{J} \\ \hat{K} \end{bmatrix}$$

- φ about $\hat{J}'$:

$$\begin{bmatrix} \hat{u} \\ \hat{v} \\ \hat{w} \end{bmatrix} = R_2(\varphi) \begin{bmatrix} \hat{I}' \\ \hat{J}' \\ \hat{K} \end{bmatrix}$$

The composite transformation can be expressed by a single composite matrix:

$$R_{32}(\vartheta, \varphi) = R_2(\varphi) \cdot R_3(\vartheta)$$

Final transformation:

$$\begin{bmatrix} \hat{u} \\ \hat{v} \\ \hat{w} \end{bmatrix} = R_{32}(\vartheta, \varphi) \begin{bmatrix} \hat{I} \\ \hat{J} \\ \hat{K} \end{bmatrix}$$

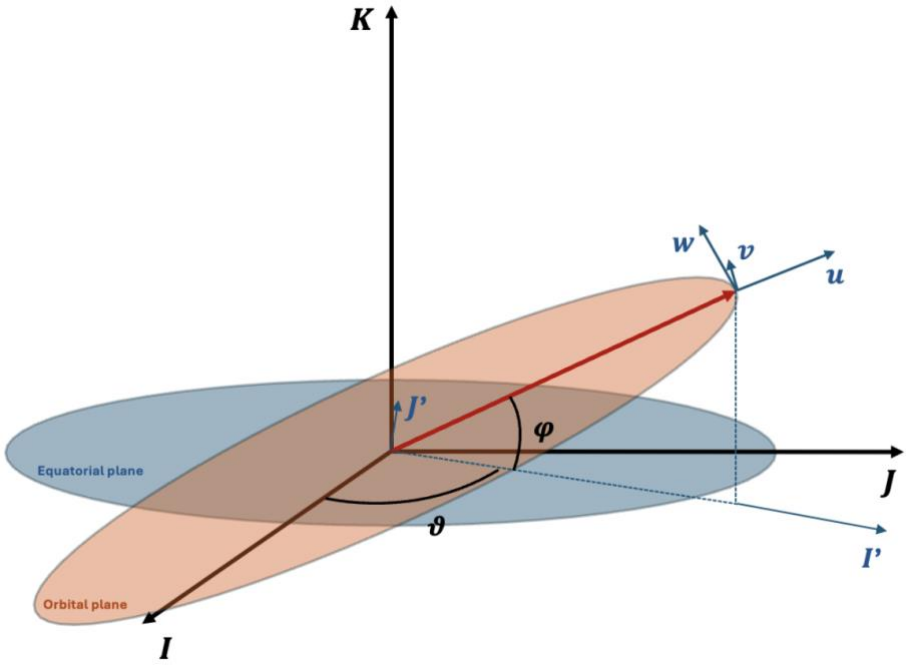

figure 11. IJK inertial frame to the ZEN orbital frame

Classical orbital elements

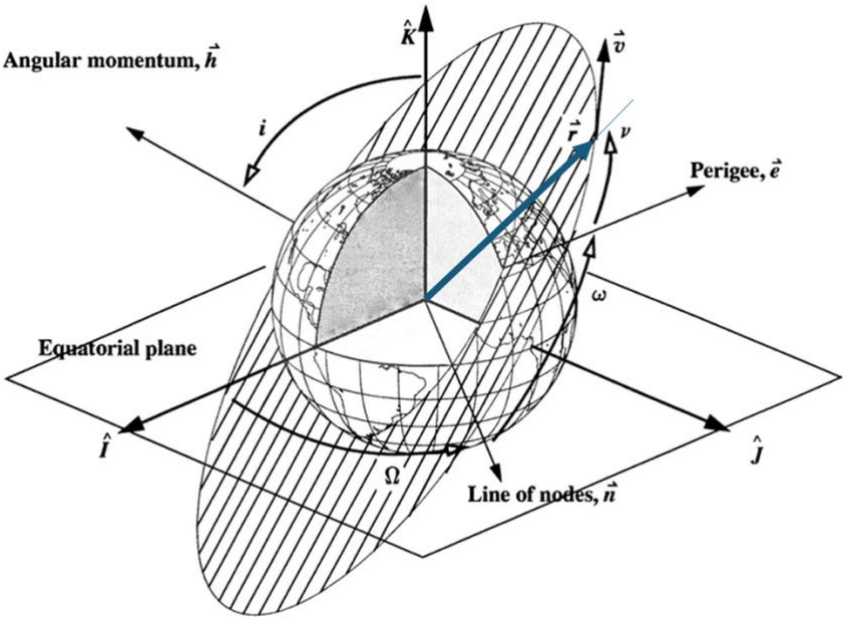

figure 12. classical orbital elements

A Keplerian trajectory is uniquely defined by six parameters known as the classical orbital elements, which provide a complete description of an orbit/trajectory:

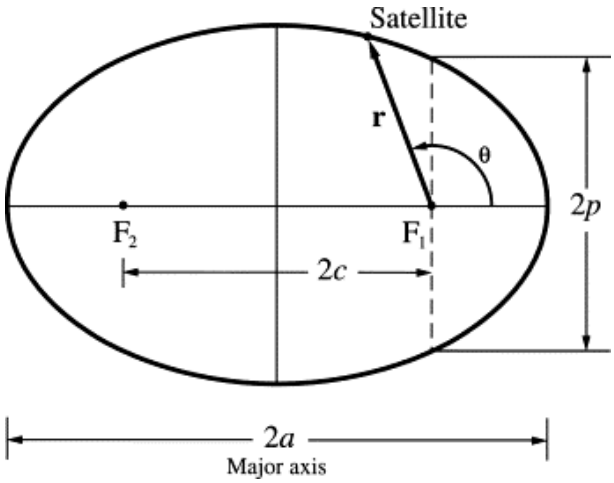

figure 13. elliptical orbit parameters (credit: Shkelzen Cakaj)

- Orbital shape definition
  - semi-major axis a

$$a = \frac{r_p + r_a}{2} = -\frac{\mu}{2\mathcal{E}}$$

  - eccentricity e

$$e = \sqrt{1 + 2\mathcal{E}\left(\frac{h}{\mu}\right)^2}$$

Alternative definition: eccentricity vector $\vec{e}$ points toward periapsis.

Governs orbital shape:

- $e = 0 \rightarrow$ circle
- $0 < e < 1 \rightarrow$ ellipse
- $e = 1 \rightarrow$ parabola
- $e > 1 \rightarrow$ hyperbola

- Orbital plane orientation
  - inclination i

    Angle between the orbital plane and reference plane (typically Earth's equatorial plane or ecliptic)

  - Right Ascension of Ascending Node – RAAN Ω

    Angle between reference direction $\vec{I}$ (e.g., vernal equinox) and the ascending node (where spacecraft crosses reference plane northward)

- Periapsis orientation
  - argument of periapsis ω

    Angle from ascending node to periapsis, measured in orbital motion direction

- Satellite position
  - true anomaly at epoch ν

    Angle between periapsis direction and current spacecraft position (changes sign when $\vec{r} \cdot \vec{V} < 0$)

    Alternative: mean anomaly (time-based equivalent for circular orbits)

Summarising:

ellipse definition	e	eccentricity	determines orbital shape
	a	semi-major axis	determines orbital size
orbital plane definition	i	inclination	refers to the inclination of the orbital plane
	Ω	Right Ascension of Ascending Node (RAAN)	angle in reference plane from Î to ascending node
ellipse orientation	ω	argument of periapsis	angle in orbital plane from ascending node to periapsis
satellite position	ν	true anomaly at epoch	angle in orbital plane from periapsis to current position at specific time t_0

table 4. element definition matrix

Perturbations

A perturbation represents a deviation from normal or expected motion. While the universe appears macroscopically as a highly regular and predictable system of motion, precise observational data reveal distinct – and sometimes inexplicable – irregularities superimposed on the mean motion of celestial bodies. The actual trajectory of an orbiting object will differ from the theoretical two-body solution due to perturbations caused by:

- additional massive bodies
- forces not accounted for in Keplerian motion

Critically, perturbations are not always negligible. Their magnitude can rival or even exceed that of the primary gravitational attraction. For instance, most interplanetary

missions would fail to reach their targets without compensation for perturbing gravitational effects.

Classification of orbital perturbations

1. By physical origin
    - gravitational perturbations:
        - third-body interactions (e.g., Moon, Sun)
        - non-spherical Earth effects (oblateness, zonal harmonics)
    - non-gravitational perturbations:
        - atmospheric drag (for LEO satellites)
        - solar radiation pressure
        - tidal friction
2. By temporal effects on Keplerian elements

type	mathematical behaviour	example causes
secular variations	linear change over time	Earth's oblateness (J_2 effect)
long-period	oscillations with period > orbital period	lunar/solar gravitational tides
short-period	oscillations with period < orbital period	atmospheric drag fluctuations

table 5. orbital perturbations classification by temporal effects

Mathematical formulation

The two-body equation of motion:

$$\ddot{\vec{r}} = -\frac{\mu}{r^2}\frac{\vec{r}}{r}$$

becomes perturbed when accounting for additional accelerations $\vec{a}_p$:

$$\ddot{\vec{r}} = -\frac{\mu}{r^2}\frac{\vec{r}}{r} + \vec{a}_p$$

This transforms the problem into a nonlinear second-order differential equation, requiring numerical methods (e.g., Encke's method, Cowell's method) for precise trajectory propagation.

Key implications for space missions

1. Orbit maintenance:
   - GEO satellites require station-keeping to counter secular drifts from J_2 effects
   - LEO satellites must compensate for atmospheric decay
2. Interplanetary trajectories:
   - gravity assists leverage third-body perturbations
   - precision navigation requires modelling > 100 perturbing accelerations
3. Orbit determination:
   - extended Kalman filters incorporate perturbation models to refine state estimates

The four primary perturbative effects considered in this analysis are:

- atmospheric drag
- Earth asphericity
- luni-solar gravitational attraction
- solar radiation pressure

Thus, the total perturbative acceleration can be expressed as the sum of these contributions:

$$\vec{a}_p = \vec{a}_{drag} + \vec{a}_{J_2} + \vec{a}_{3b} + \vec{a}_{srp} \tag{19}$$

Atmospheric drag

Atmospheric drag represents a significant external perturbation that modifies a satellite's momentum and consequently its velocity. This effect is particularly pronounced in Low Earth Orbits (LEOs) between approximately $200\ km$ and $1000\ km$ altitude. Within this altitude range, although the atmosphere is highly rarefied, sufficient atmospheric molecules remain to collide with orbiting spacecraft, generating non-negligible aerodynamic drag forces.

This perturbation results in orbital decay $(\dot{a} \neq 0)$, causing a continuous reduction in orbital altitude.

The drag acceleration $\vec{a}_d$ can be expressed as:

$$\vec{a}_d = -\frac{1}{2}\frac{C_D A}{m}\rho v_{rel}^2 \frac{\vec{v}_{rel}}{|\vec{v}_{rel}|} = -\frac{1}{2}BC\rho v_{rel}^2 \frac{\vec{v}_{rel}}{|\vec{v}_{rel}|}$$

Where:

- C_D: drag coefficient (typically ≈ 2.2 for satellites in upper atmosphere – flat plate approximation; $2.0 - 2.1$ for spherical objects)
- A: exposed cross-sectional area (dependent on satellite attitude)
- m: satellite mass
- ρ: atmospheric density (varies with altitude and is influenced by Earth's magnetic field and solar activity)
- v_{rel}: Relative velocity between satellite and atmosphere

  $$\vec{v}_{rel_{ijk}} = \vec{v}_{sc_{ijk}} - \vec{\omega}_{\oplus} \times \vec{r}_{ijk}$$

  (relative velocity calculation in IJK frame)
- BC: ballistic coefficient $\left(BC = \frac{C_D A}{m}\right)$, which characterizes a vehicle's ability to overcome air resistance during flight

Earth asphericity

The Earth's shape deviates significantly from a perfect sphere, being better approximated by a geoid – an equipotential surface of the gravitational field that optimally fits (in a least-squares sense) the global mean sea level. This irregular shape primarily results from:

- centrifugal forces due to Earth's rotation, causing an equatorial bulge (oblate spheroid shape)
- mass concentration variations (e.g., mountain ranges vs. ocean basins) creating localized gravitational anomalies

These asymmetries perturb satellite orbits through complex gravitational field variations, mathematically described by expanding the potential energy function:

$$\mho = \frac{\mu}{r}\left[1 - \sum_{l=2}^{\infty} J_l \left(\frac{R_\oplus}{r}\right)^l P_l \sin\varphi + \sum_{l=2}^{\infty}\sum_{m=1}^{l} J_l \left(\frac{R_\oplus}{r}\right)^l P_{l,m} \sin\varphi \left(C_{l,m}\cos(m\vartheta) + S_{l,m}\sin(m\vartheta)\right)\right]$$

where:

- J_l are the zonal harmonic coefficients
- P_l are the Legendre of degree l and order m

- $C_{l,m}$ are the tesseral harmonic coefficients for $l \neq m$
- $S_{l,m}$ are the sectoral harmonic coefficients
- $P_{l,m}$ are the associated polynomials of degree l and order m

Key components:

- zonal harmonics $(m = 0)$: represent latitude-dependent variations (axial symmetry)

$$\mho = \frac{\mu}{r}\left[1 - \sum_{l=2}^{\infty} J_l \left(\frac{R_\oplus}{r}\right)^l P_l \sin\varphi\right]$$

- tesseral harmonics $(l \neq m \neq 0)$: model longitudinal variations
- sectoral harmonics $(l = m)$: represent pure longitudinal bands

Perturbative accelerations

The gravitational accelerations are obtained by taking the gradient of the potential function $\Phi = \mho + \frac{\mu}{r}$ in the ZEN (Radial-Tangential-Normal) frame:

$$\left(a_J\right)_u = \frac{\partial \Phi}{\partial r}$$

$$\left(a_J\right)_v = \frac{\partial \Phi}{\partial \vartheta}\frac{1}{r cos\,\varphi}$$

$$\left(a_J\right)_w = \frac{\partial \Phi}{\partial \varphi}\frac{1}{r}$$

We can evaluate the J_n coefficients: even-numbered terms indicate symmetry about the equatorial plane, while odd-numbered terms denote asymmetry.

The J_2 coefficient demonstrates Earth's oblate spheroid shape with polar flattening.

J_3 reveals a north-south mass asymmetry, showing greater mass concentration in the northern hemisphere.

From J_4 onwards, the numerical values progressively diminish, resulting in increasingly negligible effects.

J_{12} indicates that the equator is not perfectly circular but rather elliptical.

For preliminary analysis, satisfactory propagation accuracy can be achieved by considering only the J_2 perturbation. This case involves a single associated Legendre function:

$$P_{2,0} = \frac{1}{2}(3\sin^2\varphi - 1)$$

The perturbative accelerations may be readily derived as:

$$\left(a_J\right)_u = \frac{\mu}{r^2}\left[J_2\left(\frac{R_\oplus}{r}\right)^2 \frac{1}{2}(3\sin^2\varphi - 1)\right] + \frac{\mu}{r}\left[J_2\left(\frac{R_\oplus^2}{r^3}\right)(3\sin^2\varphi - 1)\right]$$

$$\left(a_J\right)_v = 0$$

$$\left(a_J\right)_w = -\frac{\mu}{r^2}\left[J_2\left(\frac{R_\oplus}{r}\right)^2 3\sin\varphi\cos\varphi\right]$$

Solar radiation pressure (SRP)

SRP represents the momentum transfer exerted on any surface exposed to sunlight, resulting from photon impacts. This phenomenon comprises two components:

- solar wind: stream of charged particles (primarily ionised nuclei and electrons) emitted by the Sun
- solar irradiance: electromagnetic power per unit area (surface power density) across the entire electromagnetic spectrum

Maxwell's electromagnetic theory establishes that electromagnetic waves carry momentum, which transfers to illuminated surfaces. The solar radiation pressure is quantified as:

$$p_{sr} = \frac{I_{sr}}{c} = 4.5 \times 10^{-6}\frac{N}{m^2} = 4.5 \times 10^{-6} Pa$$

where I_{sr} is the solar constant and c is light speed.

The solar radiation force depends on:

- C_R: Reflectivity coefficient $(0.0 - 2.0)$, characterising surface reflectivity properties
- $A_\odot$: Sun-exposed surface area
- $\vec{r}_{sc_\odot}$: Sun-to-spacecraft position vector in J2000 frame

$$\vec{F}_{srp} = -p_{sr} C_R A_\odot \frac{\vec{r}_{sc_\odot}}{\left|\vec{r}_{sc_\odot}\right|}$$

Applying Newton's second law yields the spacecraft acceleration:

$$\vec{a}_{srp} = \frac{\vec{F}_{srp}}{m} = -\frac{p_{sr} C_R A_\odot}{m} \frac{\vec{r}_{sc_\odot}}{\left|\vec{r}_{sc_\odot}\right|}$$

This requires coordinate transformation to the ZEN frame for practical implementation.

Eclipse Conditions

During its orbital motion, the spacecraft will experience periods of partial or total eclipses when the solar radiation pressure acceleration becomes null.

To evaluate these occurrences, it is necessary to compute:

- the apparent angular sizes of relevant celestial bodies as viewed from the spacecraft $(\vartheta_\odot, \vartheta_\oplus)$
- Their angular separation γ

$$\vartheta_\odot = \arcsin\left(\frac{R_\odot}{r_{sc_\odot}}\right)$$

$$\vartheta_\oplus = \arcsin\left(\frac{R_\oplus}{r_{sc_\oplus}}\right)$$

$$\gamma = \arccos\left(\frac{\vec{r}_{sc_\odot}\vec{r}_{sc_\oplus}}{r_{sc_\odot} r_{sc_\oplus}}\right)$$

The illumination function L accounts for orbital eclipses:

$$L = \begin{cases} 1 & if \quad \gamma - \vartheta_\odot > \vartheta_\oplus & full\ illumination \\ 0 & if \quad \vartheta_\oplus > \gamma + \vartheta_\odot & full\ eclipse \\ 1 - \dfrac{\vartheta_\oplus^2}{\vartheta_\odot^2} & if \quad \vartheta_\odot - \vartheta_\oplus \geq \gamma \ or \ \gamma \geq \vartheta_\odot + \vartheta_\oplus & partial\ eclipse \\ 1 - \dfrac{A + B - C}{\pi \vartheta_\odot^2} & if \quad else & penumbral\ region \end{cases}$$

with auxiliary terms:

$$A = \vartheta_\oplus^2 \arccos\left(\frac{\gamma^2 + \vartheta_\oplus^2 - \vartheta_\odot^2}{2\gamma\vartheta_\oplus}\right)$$

$$B = \vartheta_{\odot}^2 \arccos\left(\frac{\gamma^2 + \vartheta_{\odot}^2 - \vartheta_{\oplus}^2}{2\gamma\vartheta_{\oplus}}\right)$$

$$C = \frac{1}{2}\sqrt{(-\gamma + \vartheta_{\oplus} + \vartheta_{\odot})(\gamma + \vartheta_{\oplus} - \vartheta_{\odot})(\gamma - \vartheta_{\oplus} + \vartheta_{\odot})(\gamma + \vartheta_{\oplus} + \vartheta_{\odot})}$$

The complete acceleration model becomes:

$$\vec{a}_{srp} = L\frac{\vec{F}_{srp}}{m} = -L\frac{p_{sr}C_R A_{\odot}}{m}\frac{\vec{r}_{sc_{\odot}}}{\left|\vec{r}_{sc_{\odot}}\right|}$$

Lunisolar effect

The combined gravitational influence of the Sun and Moon on Earth drives the precession of the equinoxes – a slow gyration of Earth's rotational axis with a period of approximately $25.772\ years$. This phenomenon alters the alignment of Earth's axis relative to the celestial sphere.

The perturbative acceleration due to the i-th celestial body (Sun or Moon) is given by:

$$\vec{a}_{3b_i} = \mu_i\left(\frac{\vec{r}_{sc_i}}{r_{sc_i}^3} - \frac{\vec{r}_i}{r_i^3}\right)$$

where:

- μ_i is the gravitational parameter of the i-th body
- $\vec{r}_{sc_i}$ is the position vector of the satellite relative to the i-th body
- $\vec{r}_i$ is the position vector of the i-th body relative to Earth

Physical interpretation

- direct effect (first term): acceleration induced on the satellite by the third body's gravity
- indirect effect (second term): acceleration exerted on Earth by the third body, which indirectly perturbs the satellite's orbit through Earth's resultant motion

Fifth Chapter

The implemented OCP

In this paragraph, what has been seen in the theory of the previous chapters is adapted to the case under consideration.

The state vector is composed of:

$$\vec{x} = \{r, \vartheta, \varphi, u, v, w, m\} \tag{20}$$

Starting from this, it is possible to associate each variable with a costate or adjoint variable.

The augmented state vector is defined as:

$$\vec{y} = \{r, \vartheta, \varphi, u, v, w, m, \lambda_r, \lambda_\vartheta, \lambda_\varphi, \lambda_u, \lambda_v, \lambda_w, \lambda_m\} \tag{21}$$

First, a two-body system in the presence of perturbative actions was considered, whose dynamics are described by the following equations:

$$\begin{cases} \dfrac{d\vec{r}}{dt} = \vec{v} \\ \dfrac{d\vec{v}}{dt} = -\dfrac{\vec{\mu}}{r^3}\vec{r} + \dfrac{\vec{T}}{m} \\ \dfrac{dm}{dt} = -\dfrac{\vec{T}}{c} \end{cases}$$

The equations of motion (EoM) thus take the form:

$$\begin{cases} \dfrac{dr}{dt} = u \\ \dfrac{d\vartheta}{dt} = \dfrac{v}{r\cos\varphi} \\ \dfrac{d\varphi}{dt} = \dfrac{w}{r} \\ \dfrac{du}{dt} = -\dfrac{\mu}{r^2} + \dfrac{v^2}{r} + \dfrac{w^2}{r} + \dfrac{T_u}{m} + (a_p)_u \\ \dfrac{dv}{dt} = -\dfrac{uv}{r} + \dfrac{vw}{r}\tan\varphi + \dfrac{T_v}{m} + (a_p)_v \\ \dfrac{dw}{dt} = -\dfrac{uw}{r} - \dfrac{v^2}{r}\tan\varphi + \dfrac{T_w}{m} + (a_p)_w \\ \dfrac{dm}{dt} = -\dfrac{T}{c} \end{cases}$$

where:

$$T: \begin{cases} T_u = T\sin\alpha_T & = & T\dfrac{\lambda_u}{\lambda_V} \\ T_v = T\cos\alpha_T\cos\beta_T & = & T\dfrac{\lambda_v}{\lambda_V} \\ T_w = T\cos\alpha_T\sin\beta_T & = & T\dfrac{\lambda_w}{\lambda_V} \end{cases}$$

with $\lambda_V = \sqrt{\lambda_u^2 + \lambda_v^2 + \lambda_w^2}$ primer vector.

The Hamiltonian for the OCP under consideration takes the form:

$$\mathcal{H} = \vec{\lambda}^T \cdot \vec{f} = \sum_{i=1}^{2n} \lambda_i f_i =$$

$$= \lambda_r u + \lambda_\vartheta \frac{v}{r cos\varphi} + \lambda_\varphi \frac{w}{r} +$$

$$+\lambda_u \left[-\frac{\mu}{r^2} + \frac{v^2}{r} + \frac{w^2}{r} + \frac{T_u}{m} + \left(a_p\right)_u \right] + \lambda_v \left[-\frac{uv}{r} + \frac{vw}{r}\tan\varphi + \frac{T_v}{m} + \left(a_p\right)_v \right] +$$

$$+\lambda_w \left[-\frac{uw}{r} - \frac{v^2}{r}\tan\varphi + \frac{T_w}{m} + \left(a_p\right)_w \right] + \lambda_m \left(-\frac{T}{c} \right) \tag{22}$$

The terms containing thrust can be grouped:

$$\frac{1}{m}(\lambda_u T_u + \lambda_v T_v + \lambda_w T_w) + \lambda_m \left(-\frac{T}{c} \right) = \vec{\lambda}_V^T \frac{\vec{T}}{m} - \lambda_m \frac{T}{c} = \frac{T}{m}\left(\vec{\lambda}_V^T \frac{\vec{T}}{T} - \lambda_m \frac{m}{c} \right) = \frac{T}{m} SF$$

A new parameter has thus been derived, the switching function:

$$SF = \lambda_V - \lambda_m \frac{m}{c} \tag{23}$$

It works somewhat like an engine switch, in fact:

$$T = \begin{cases} 0 & if\ SF < 0 \\ T_{MAX} & if\ SF > 0 \end{cases}$$

The Hamiltonian can therefore be rewritten as:

$$\mathcal{H} = \lambda_r u + \lambda_\vartheta \frac{v}{r cos\varphi} + \lambda_\varphi \frac{w}{r} +$$

$$+\lambda_u \left[-\frac{\mu}{r^2} + \frac{v^2}{r} + \frac{w^2}{r} + \left(a_p\right)_u \right] + \lambda_v \left[-\frac{uv}{r} + \frac{vw}{r}\tan\varphi + \left(a_p\right)_v \right]$$

$$+ \lambda_w \left[-\frac{uw}{r} - \frac{v^2}{r}\tan\varphi + \left(a_p\right)_w \right] + \frac{T}{m} SF$$

The optimal values for the thrust angles were obtained by differentiating the Hamiltonian with respect to the angles themselves [10]:

$$\frac{\partial \mathcal{H}}{\partial \alpha_T} = \lambda_u \cos\alpha_T - (\lambda_v \cos\beta_T + \lambda_w \sin\beta_T)\sin\alpha_T = 0$$

$$\frac{\partial \mathcal{H}}{\partial \beta_T} = -\lambda_v \sin\beta_T + \lambda_w \cos\beta_T = 0$$

After various manipulations, the optimal thrust directions are obtained:

$$\sin\alpha_T = \frac{\lambda_u}{\lambda_V} \tag{24}$$

$$\cos\alpha_T \cos\beta_T = \frac{\lambda_v}{\lambda_V} \tag{25}$$

$$\cos\alpha_T \sin\beta_T = \frac{\lambda_w}{\lambda_V} \tag{26}$$

which coincide with the direction cosines of the primer vector.

The ODEs for the adjoint variables are obtained using the following relation:

$$\frac{d\lambda_\cdot}{dt} = -\frac{\partial \mathcal{H}}{\partial \cdot}$$

(for simplicity of calculation, it was chosen to neglect the variations of thrust with respect to the other variables. Since the thruster does not appear to be a function of position, ergo the thrust is always constant if the engine is on, we are not simply 'neglecting', but the variation itself is nil: $\frac{dT}{dr}, \frac{dT}{d\vartheta}, \frac{dT}{d\varphi} = 0$)

Specifically:

$$\frac{d\lambda_r}{dt} = -\frac{\partial \mathcal{H}}{\partial r} = \frac{1}{r^2}\left[\lambda_\vartheta \frac{v}{\cos\varphi} + \lambda_\varphi w + \lambda_u\left(-2\frac{\mu}{r} + v^2 + w^2\right) + \lambda_v(-uv + vw\tan\varphi)\right.$$
$$\left. + \lambda_w(-uw - v^2\tan\varphi) - \lambda_u\frac{\partial(a_p)_u}{\partial r} - \lambda_v\frac{\partial(a_p)_v}{\partial r} - \lambda_w\frac{\partial(a_p)_w}{\partial r}\right]$$

$$\frac{d\lambda_\vartheta}{dt} = -\frac{\partial \mathcal{H}}{\partial \vartheta} = -\lambda_u\frac{\partial(a_p)_u}{\partial \vartheta} - \lambda_v\frac{\partial(a_p)_v}{\partial \vartheta} - \lambda_w\frac{\partial(a_p)_w}{\partial \vartheta}$$

$$\frac{d\lambda_\varphi}{dt} = -\frac{\partial \mathcal{H}}{\partial \varphi} = \frac{1}{r\cos^2\varphi}(-\lambda_\vartheta v\sin\varphi - \lambda_v vw + \lambda_w v^2) - \lambda_u \frac{\partial (a_p)_u}{\partial \varphi} - \lambda_v \frac{\partial (a_p)_v}{\partial \varphi} - \lambda_w \frac{\partial (a_p)_w}{\partial \varphi}$$

$$\frac{d\lambda_u}{dt} = -\frac{\partial \mathcal{H}}{\partial u} = -\lambda_r + \lambda_v \frac{v}{r} + \lambda_w \frac{w}{r}$$

$$\frac{d\lambda_v}{dt} = -\frac{\partial \mathcal{H}}{\partial v} = \frac{1}{r}\left[-\lambda_\vartheta \frac{1}{\cos\varphi} - \lambda_u 2v + \lambda_v(u - w\tan\varphi) + \lambda_w 2v\tan\varphi\right]$$

$$\frac{d\lambda_w}{dt} = -\frac{\partial \mathcal{H}}{\partial w} = \frac{1}{r}(-\lambda_\varphi - \lambda_u 2w + \lambda_v v\tan\varphi + \lambda_w u)$$

$$\frac{d\lambda_m}{dt} = -\frac{\partial \mathcal{H}}{\partial m} = -\lambda_u \frac{\partial (a_p)_u}{\partial m} - \lambda_v \frac{\partial (a_p)_v}{\partial m} - \lambda_w \frac{\partial (a_p)_w}{\partial m} + \lambda_V \frac{T}{m^2}$$

Case study

The objective of this thesis is to demonstrate the ability to reach the orbit of a generic debris object while reducing the cost of the manoeuvre.

It is assumed that the launcher releases the satellite at an initial altitude of $h_i = 500\ km$, and that manoeuvres are performed to reach the chosen debris. To simulate a realistic scenario, the propulsion characteristics of the main spacecraft were based on the technical specifications of modern ion thrusters, suitable as primary propulsion systems for medium-sized satellites.

The engine characteristics are summarised in the following table, which also includes the satellite's initial mass:

thrust T	$50\ mN$
specific impulse I_{sp}	$\sim 3000\ s$
power P	$0.5 \div 2.3\ kW$
initial mass m_0	$500\ kg$

table 6. engine characteristics

The thrust and specific impulse are considered constant for the entire mission duration (assuming a complete absence of thrust regulation), as described in the bang-bang control.

The assumption of an initial mass of $500\,kg$ was made for potential future developments where multiple manoeuvres could be combined to retrieve a larger number of debris objects or to equip the satellite with instrumentation suitable for possible in-orbit repairs.

An important observation must be made: in the current study, the use of a debris removal system is not assumed. However, this does not alter the present study, as it primarily focuses on the transfer to the debris and not on the actual de-orbiting operation.

The case study is set in the intermediate region of the LEO environment, a typical operational domain for this type of spacecraft. It is assumed that the launcher leaves the satellite at an initial altitude of $500\,km$, belonging to one of the most crowded bands, and that it must perform manoeuvres to capture a space debris object.

For the selection of the debris, three Python scripts were created that work together to retrieve, filter, and analyse the orbital data of space debris present in the Space-Track.org database.

In the main file, restrictive conditions are entered on the orbital parameters of interest; in this case, it was chosen to operate at an altitude of 520 km with a tolerance of 5 km, an inclination of 0°±10°, and nearly circular orbits (i.e., eccentricity less than 0.01).

An example of output related to the debris is:

```
[INFO] Detriti trovati con altitudine 520 ± 5 km, inclinazione 0 ± 10°, eccentricità ≤ 0.01: 3

Nome: HETE 2, Altitudine: 519.92 km, Inclinazione: 1.94°, Eccentricità: 0.00206, Epoca: 2024-01-05T12:11:07.777824
Nome: NULION, Altitudine: 524.22 km, Inclinazione: 5.01°, Eccentricità: 0.00038, Epoca: 2023-12-07T20:16:30.125568
Nome: POEM, Altitudine: 516.83 km, Inclinazione: 9.95°, Eccentricità: 0.00274, Epoca: 2025-07-14T07:34:08.935680
```

figure 14. debris output example

As can be seen, the name of the debris, its altitude, inclination, eccentricity, and the temporal moment to which the orbital data refer are returned in order.

The more recent the data, the better the accuracy of the calculations; indeed, the orbital parameters remain more or less constant for a short period around the epoch, as the orbits are subject to atmospheric perturbations or other effects that cause alterations.

Once the debris of interest are found, the file used to obtain the NORAD ID code of the debris from its name is used.

This code is a unique numerical identifier assigned to each artificial object in orbit around the Earth by the North American Aerospace Defence Command.

For example, it might be: "The NORAD_CAT_ID of 'POEM' is: 52939."

Using the website: [https://www.n2yo.com/satellite/?s=52939#results] (updated to 16/07/2025), it is possible to see the satellite's ground track and its orbital parameters.

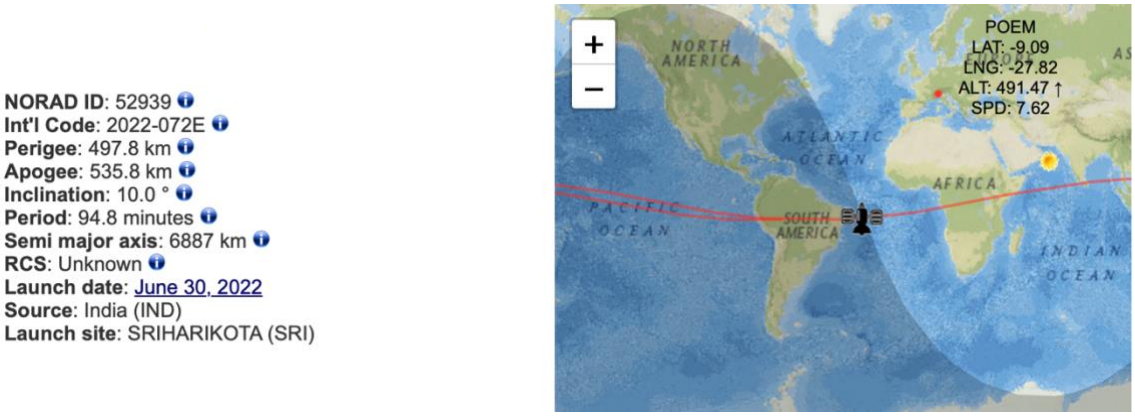

figure 15. POEM's orbital parameters and ground track

Finally, the debris orbit is simulated over time.

Thus, the debris orbit is propagated, and all necessary parameters are derived using the Two-Line Elements (TLE) from Space-Track.

TLEs are a standardised format of orbital data used to describe the trajectory of satellites, space debris, or other objects in orbit around the Earth. They consist of two lines of text and contain all the parameters needed to calculate an object's position and velocity at a given time using the SGP4/SDP4 mathematical model.

```
--- TLE scaricati da Space-Track ---
Linea 1: 1 52939U 22072E   25196.89139357  .00004669  00000-0  17411-3 0  9991
Linea 2: 2 52939   9.9521  97.1795 0027600 260.0409  99.6690 15.18737635168202
```

figure 16. POEM TLE

The second line includes:

inclination	$9.9521°$
Right Ascension of Ascending Node	$97.1795°$
eccentricity	0.00276
argument of periapsis	$260.0409°$
mean anomaly	$99.6690°$
mean motion	$15.18737635\ rev/day$
revolutions number	16820

table 7. POEM TLE

Once all the data were obtained, it was possible to represent the debris orbit:

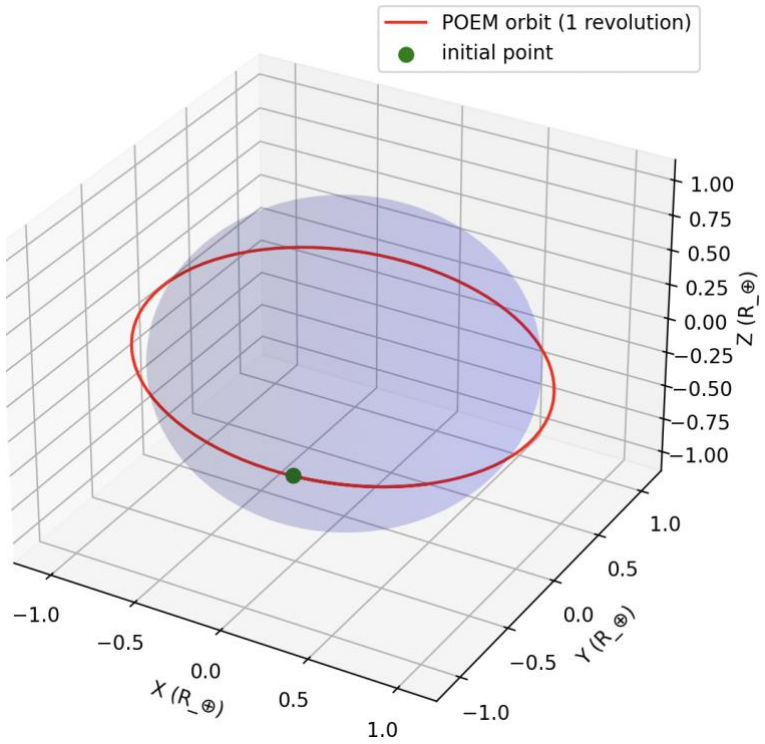

figure 17. POEM orbit

To better visualise the variation in longitude and latitude, it is useful to switch to a 2D graph as a function of normalised altitude:

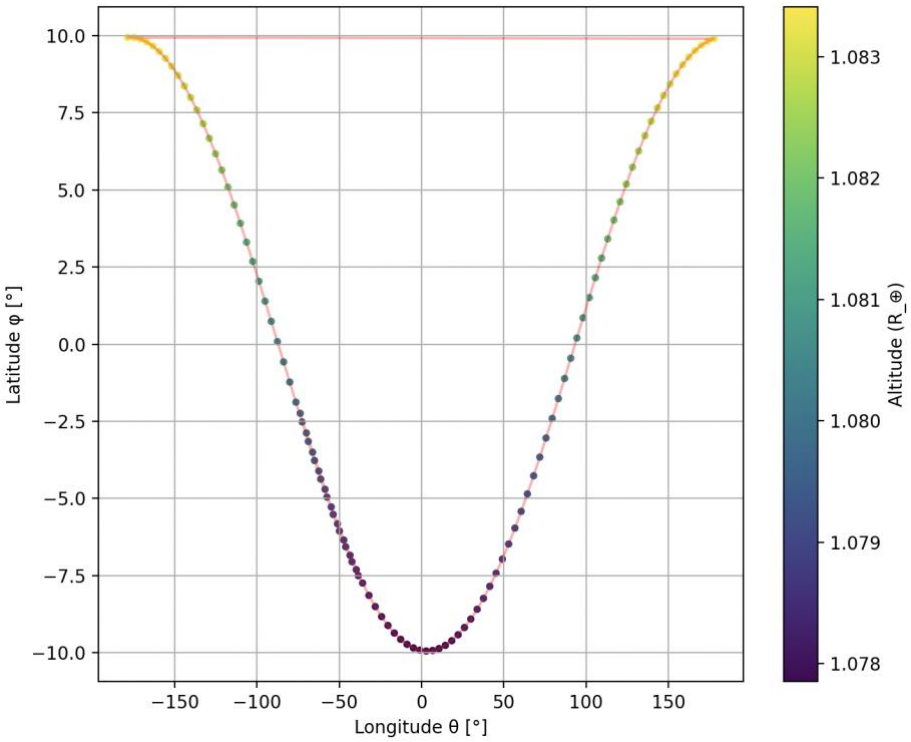

figure 18. latitude-longitude 2D graph

Returning to the initial problem, the necessary manoeuvres for the satellite to reach the target must be evaluated:

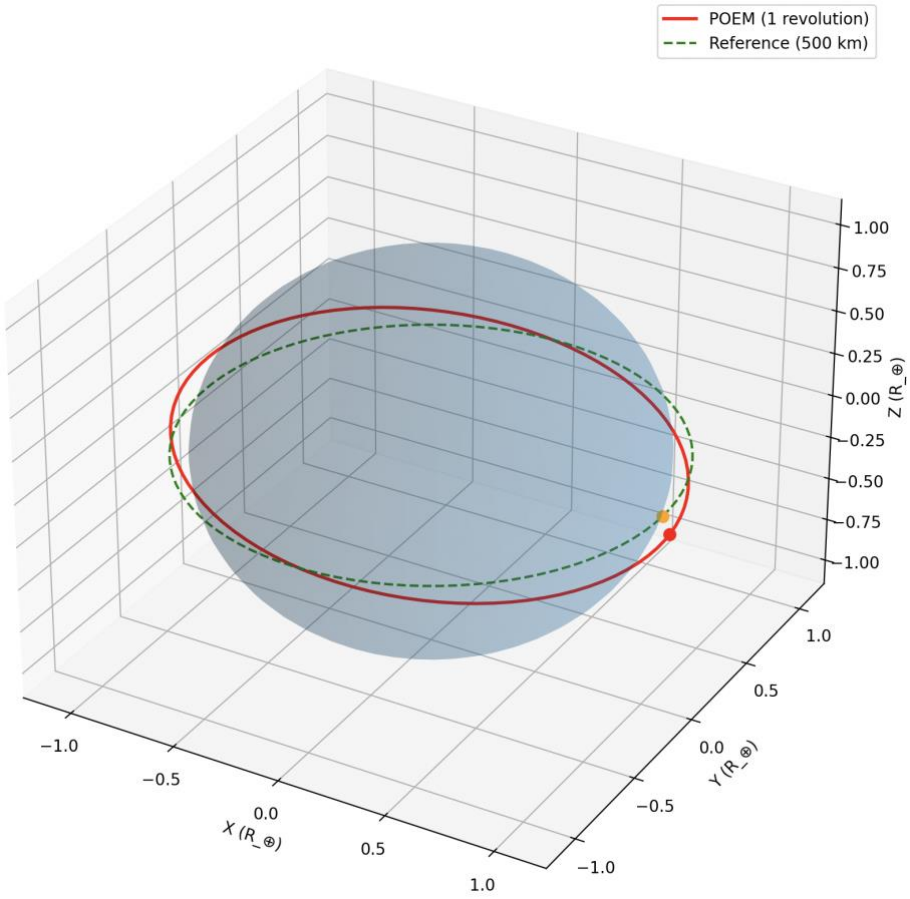

figure 19. comparison between reference and POEM orbit

Starting from an initial orbit of $500\ km$, the debris POEM must be reached.

First, the problem was analysed from the perspective of traditional orbital mechanics, i.e., through a Hohmann transfer.

Recalls on orbital manoeuvres

A generic transfer can take the following form:

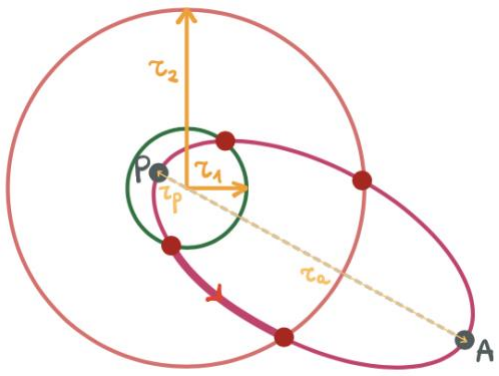

figure 20. generic transfer

How can we move from orbit r_1 to orbit r_2?

If we start from orbit r_1, the transfer orbit must pass through that radius. Therefore, the minimum radius of the transfer orbit must be less than or equal to r_1: $r_p \leq r_1$.

Similarly, the transfer orbit must, at a minimum, reach the radius r_2 to arrive at a circular orbit of that radius: $r_a \geq r_2$.

In contrast, the Hohmann transfer has the most extreme conditions, i.e.:

$$r_p = r_1 \text{ and } r_a = r_2$$

This way, the transfer orbit is tangent to both circular orbits:

- at the periapsis, it touches the circle of radius r_1
- at the apoapsis, it touches the circle of radius r_2

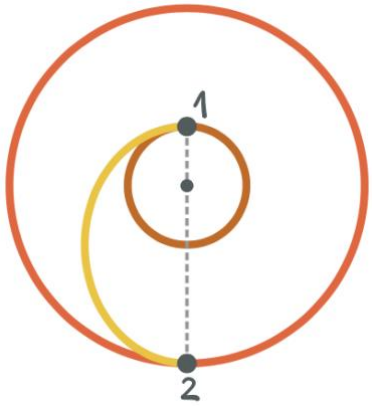

figure 21. Hohmann transfer

At both periapsis and apoapsis, the velocity is entirely tangential – there is no radial component.

Velocity Analysis

Let:

- V_{c_1} = velocity on the circular orbit at point 1
- V_{H_1} = velocity on the Hohmann transfer orbit at point 1

Since $V_{H_1} > V_{c_1}$, if we want to increase the orbital radius, the velocities will have the same direction.

At point 2:

- V_{H_2} = velocity on the Hohmann transfer orbit
- V_{c_2} = velocity on the circular orbit at radius r_2

Here, $V_{c_2} > V_{H_2}$.

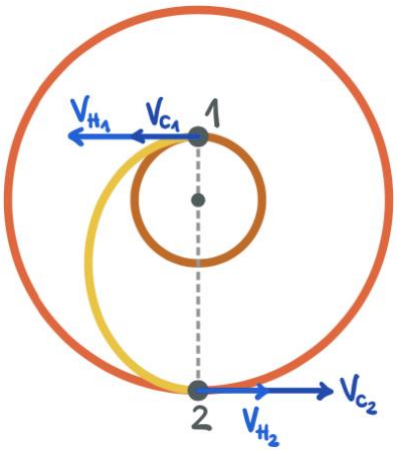

figure 22. velocity scheme

Cost of a Hohmann Transfer

If we are in a circular orbit of radius r_1, we can immediately calculate the corresponding velocity using the energy equation:

$$\mathcal{E} = -\frac{\mu}{2a}$$

Since it's a circular orbit, $a = r$, so:

$$\mathcal{E}_1 = -\frac{\mu}{2r_1} = \frac{V_{c_1}^2}{2} - \frac{\mu}{r_1} \implies V_{c_1} = \sqrt{\frac{\mu}{r_1}}$$

Similarly, for the second orbit:

$$\mathcal{E}_2 = -\frac{\mu}{2r_2} = \frac{V_{c_2}^2}{2} - \frac{\mu}{r_2} \implies V_{c_2} = \sqrt{\frac{\mu}{r_2}}$$

The farther we are from the attracting body, the slower we orbit.

For the Hohmann transfer, we can also use the energy equation, where the semi-major axis is:

$$a = \frac{r_1 + r_2}{2}$$

Thus:

$$\mathcal{E}_H = -\frac{\mu}{r_1 + r_2} = \frac{V_{H_1}^2}{2} - \frac{\mu}{r_1} = \frac{V_{H_2}^2}{2} - \frac{\mu}{r_2}$$

The Hohmann velocities are:

$$V_{H_1} = \sqrt{2\mu\left(\frac{1}{r_1} - \frac{1}{r_1+r_2}\right)} \text{ and } V_{H_2} = \sqrt{2\mu\left(\frac{1}{r_2} - \frac{1}{r_1+r_2}\right)}$$

The total cost of the transfer is:

$$\Delta V_1 = \left|V_{H_1} - V_{c_1}\right| \text{ and } \Delta V_2 = \left|V_{c_2} - V_{H_2}\right|$$

(The absolute value is used because ΔV is "paid" for both braking and acceleration)

Numerical Example

Given the values:

V_{c_1}	$7.616556585247121\,\frac{\text{km}}{\text{s}}$
V_{c_2}	$7.607703981255776\,\frac{\text{km}}{\text{s}}$
V_{H_1}	$7.6209841726492495\,\frac{\text{km}}{\text{s}}$
V_{H_2}	$7.603278967659793\,\frac{\text{km}}{\text{s}}$
ΔV_1	$0.004427587402128452\,\frac{\text{km}}{\text{s}}$
ΔV_2	$0.004425013595983351\,\frac{\text{km}}{\text{s}}$
ΔV_{tot}	$0.008852600998111804\,\frac{\text{km}}{\text{s}}$
T_H	$2839.024822294727\ \text{s}$

table 8. Hohmann transfer results

During the work on this thesis, thanks to the invaluable assistance of supervisor Luigi Mascolo, it was possible to implement a GUI that allowed for 'tweaking' the parameters to achieve the desired solution:

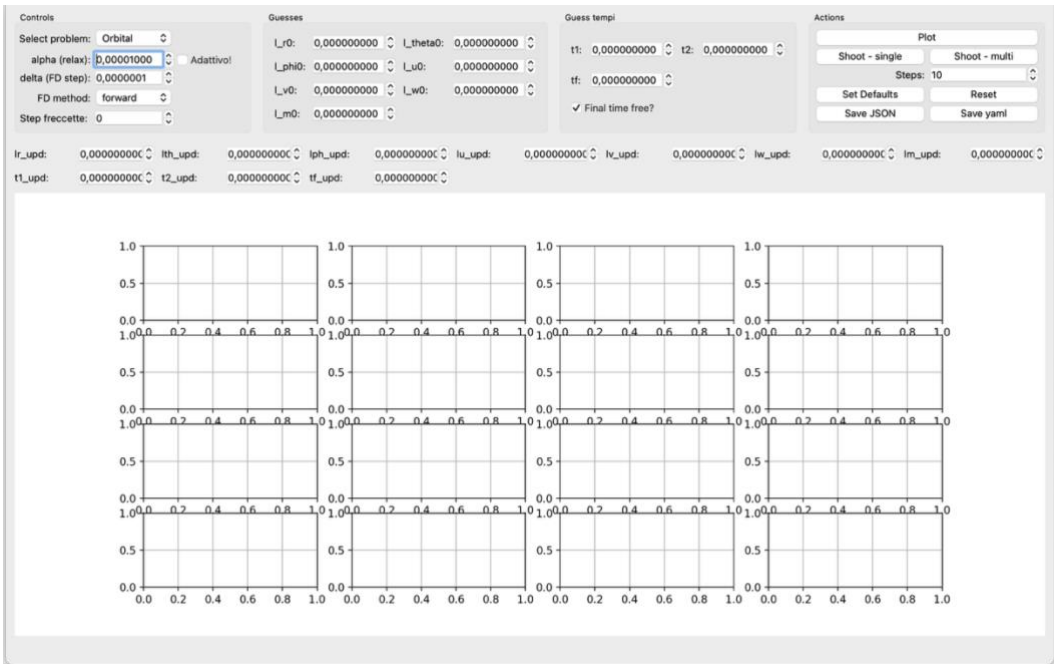

figure 23. GUI interface

Knowing that a manoeuvre causing an increase in the semi-major axis was required, priority was given to the costates related to radius and tangential velocity, namely λ_r and λ_v.

Regarding the final simulation time, the reference chosen was the dimensionless Hohmann orbit time: $T_{H_{adim}} = 2 \times 3.5186837801108704$.

In general, to work with quantities that did not differ by too many orders of magnitude and avoid numerical instability issues, the following dimensionless units were adopted:

length unit	$6371\ km$
gravitational parameter	$398600 \frac{km^3}{s^2}$
velocity unit	$\sqrt{\frac{\mu_\oplus}{R_\oplus}} = 7.909766019 \frac{km}{s}$
time unit	$\frac{R_\oplus}{v_c} = 805.4577423\ s$
acceleration unit	$\frac{v_c^2}{R_\oplus} = 0.009820239 \frac{km}{s^2}$
mass unit	$500\ kg$
thrust unit	$M \times A = 4.910119801 \frac{kg \cdot km}{s^2}$

table 9. dimensionless units

To achieve the required semi-major axis variation, the manoeuvre was subdivided into a series of sub-manoeuvres, each with a fixed increment of $250\ m$.

The switching function follows a $[1 - 0 - 1]$ pattern, meaning an alternation between engine on (1) and engine off (0).

Once a sub-manoeuvre is completed, orbital propagation is performed – i.e., the numerical integration of the equations of motion – to simulate the temporal evolution of the satellite's orbit under various forces.

The propagation time was set to two full orbital periods to:

- verify the model's consistency
- isolate the effects of perturbations from those of propulsion
- calculate the new initial conditions for the optimisation problem

Additionally, this engine-off period helps prevent overheating and respects continuous burn-time limitations.

Case without perturbations

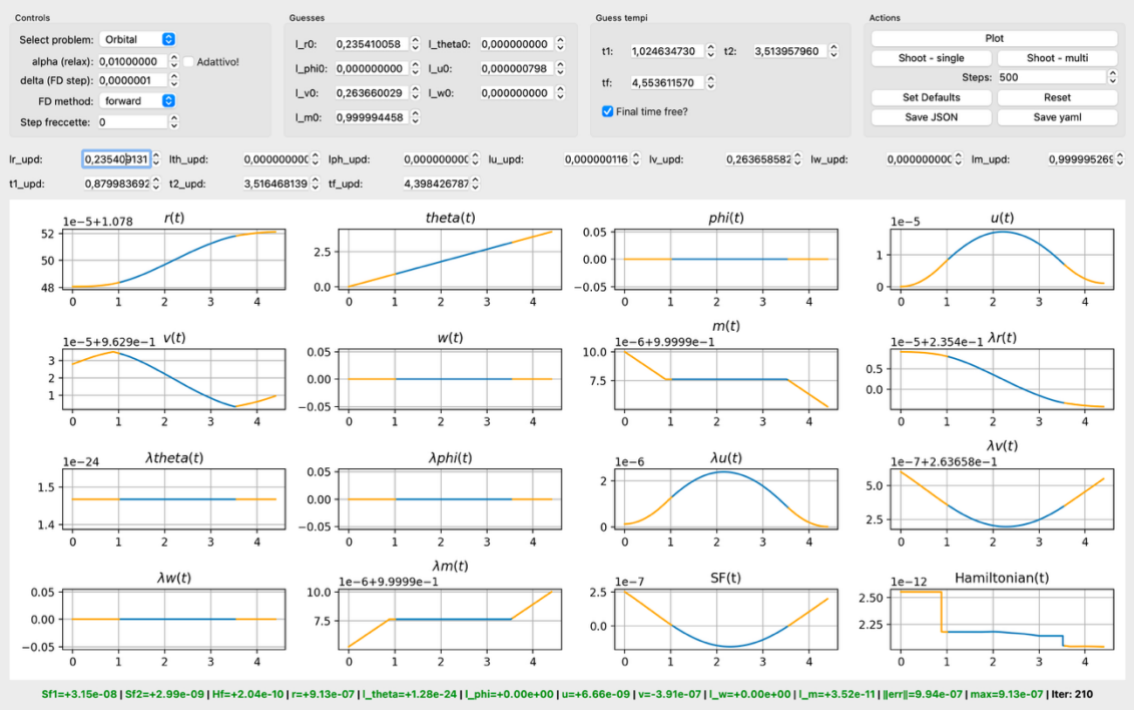

figure 24. case without perturbations

Subsequently, perturbations were introduced. Specifically, the following were considered:

- atmospheric drag
- lunisolar gravitational attraction
- solar radiation pressure

This section details specific modifications or implementations for the case under study.

The density was calculated using the MSIS (Mass Spectrometer and Incoherent Scatter Radar) model for a specified time and altitude range.

An example output is:

time_sec_since_start	altitude_km	density_kg_m3
0.0	100.000	5.410220×10^{-07}
1800.0	250.000	4.775276×10^{-11}
3600.0	500.000	3.138841×10^{-13}
21600.0	600.000	4.642457×10^{-14}

table 10. density grid output example

From this table, bilinear interpolation was used to estimate density at a given altitude/time.

The drag acceleration was then computed in IJK coordinates and converted to ZEN coordinates.

For simplicity, the Sun and Moon were assumed to follow circular orbits, as using precise ephemerides for exact relative positions (Earth-Sun or Earth-Moon) would have compromised computational speed and robustness.

A similar approach was taken for solar radiation pressure.

First full iteration with perturbations

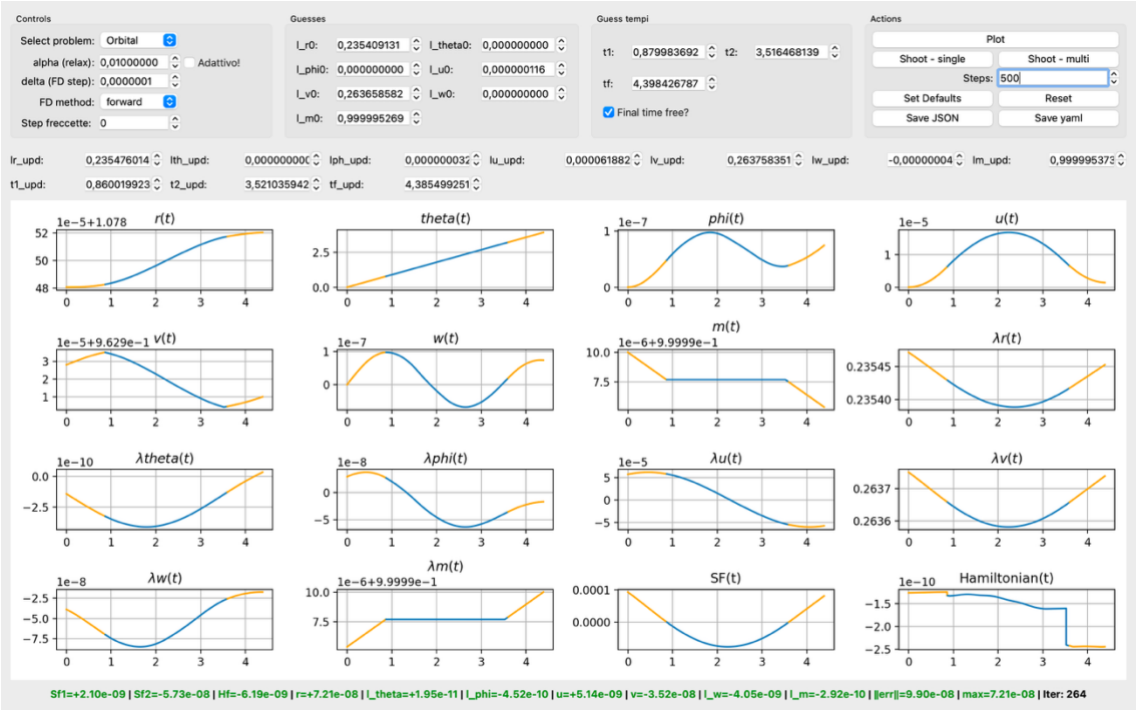

figure 25. case with perturbations

As can be observed, there are no major variations in the costates. The parameter most affected is the one related to velocity, consistent with the fact that perturbations primarily influence accelerations.

Subsequently, orbital propagation was performed, yielding the following output:

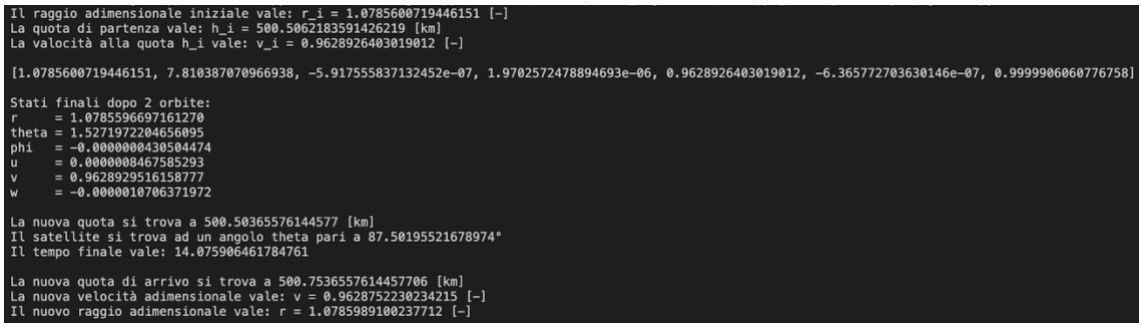

figure 26. propagation results

Examining the new starting altitude, a decrease compared to the previous final altitude is noted. This reduction is consistent with the presence of perturbations.

Results

By utilising another Python script, it was possible to derive the orbital parameters from the results obtained in the last convergence:

semi-major axis	6887.224673 km
eccentricity	0.000002
inclination	9.9°
Right Ascension of Ascending Node	208.316911°
argument of periapsis	82.999973°
mean anomaly	82.719180°
orbital period	94.803931 min
mean motion	15.18924358 rev/day
revolutions number	16820

table 11. spacecraft last parameters

The final position to be reached by the spacecraft will correspond to the debris orbit, and the transfer phase will be considered complete once these final conditions are met. In this scenario, this will indicate that the spacecraft has completed insertion into the desired orbit and achieved rendezvous with the debris.

It is specified that, of course, the capture of the debris will require a certain amount of time for completion. However, since studying the specifics of this operation is not the focus of this thesis, this detail is disregarded, assuming that by the time the spacecraft reaches the debris, this activity will be completed within a reasonably short timeframe.

Using the results obtained, it was possible to plot the evolution of:

dimensionless radius

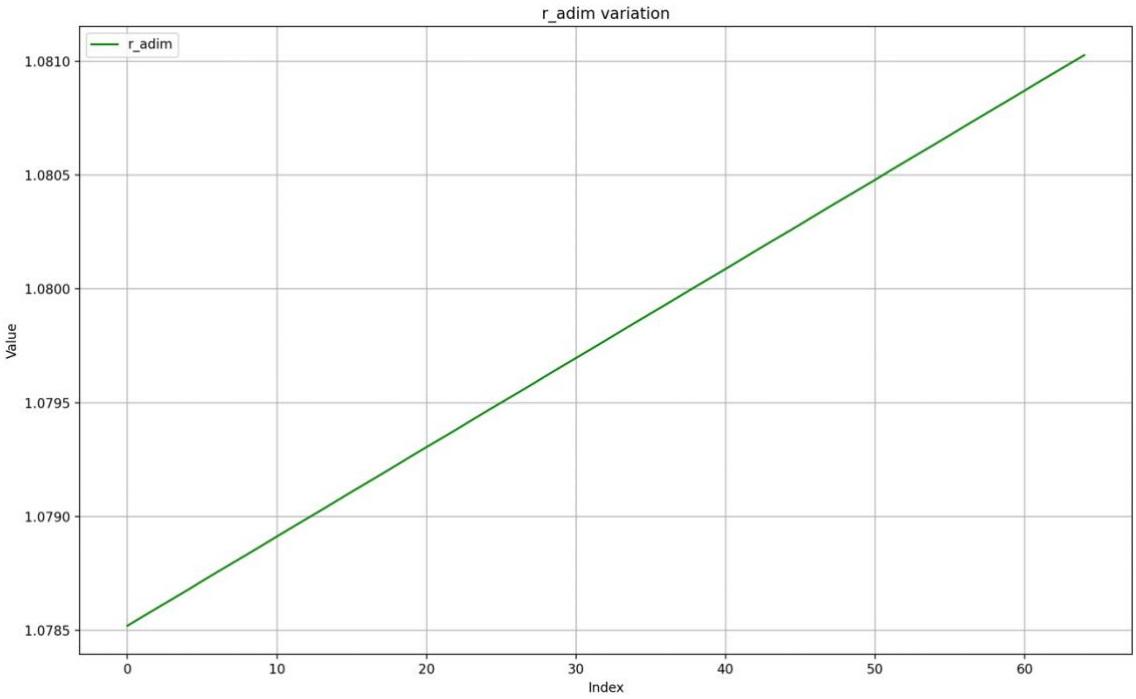

figure 27. radius variation

Regarding the propagated dimensionless radius, it was necessary to perform an analysis over multiple orbits to validate the consistency of the method used:

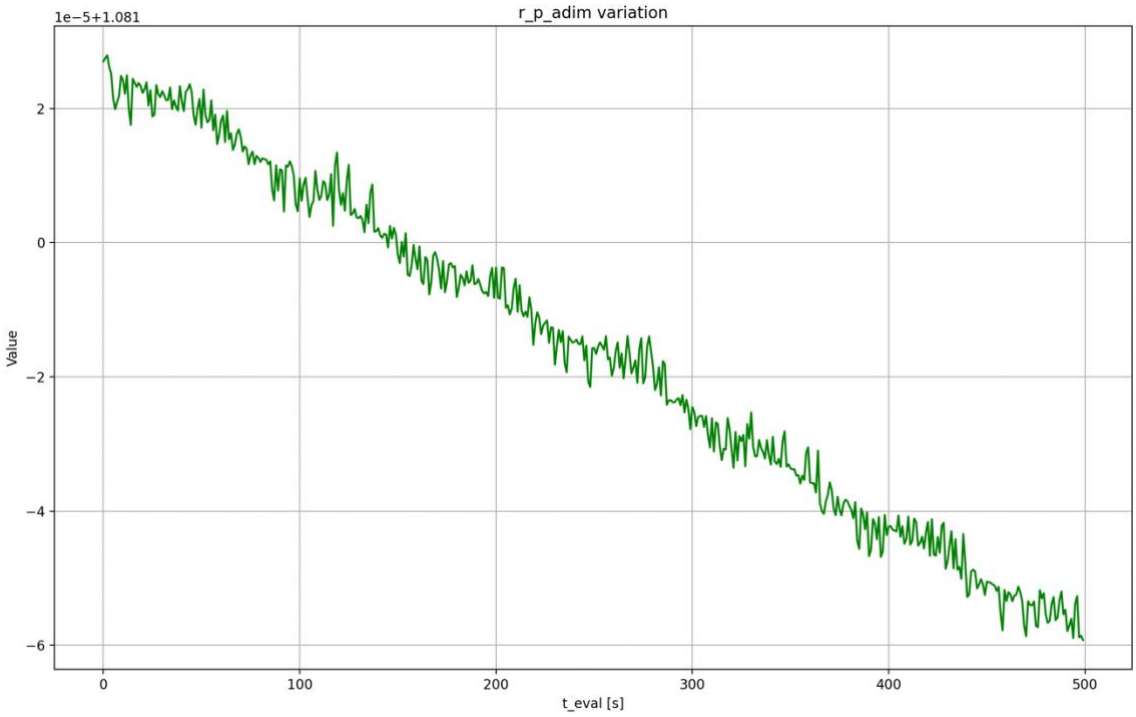

figure 28. propagated dimensionless radius variation

By descending further in altitude and increasing the number of propagated orbits, it is possible to observe how the satellite progresses toward the deorbiting altitude:

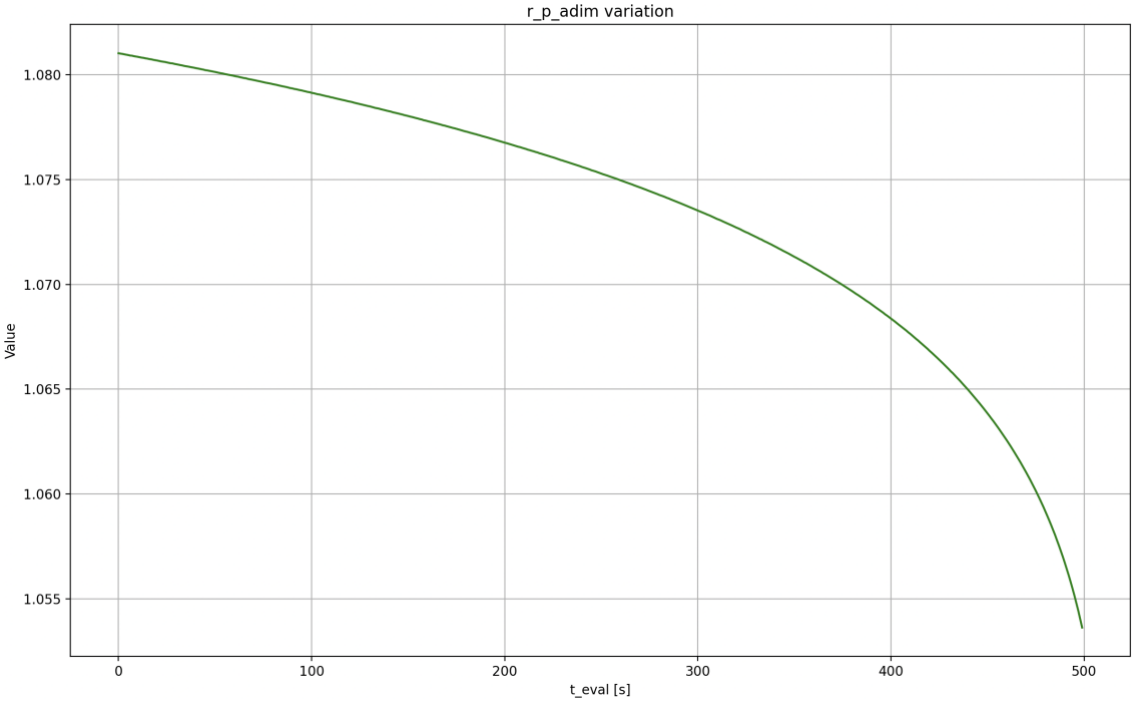

figure 29. descending radius

Comparison between dimensionless radius and propagated dimensionless radius:

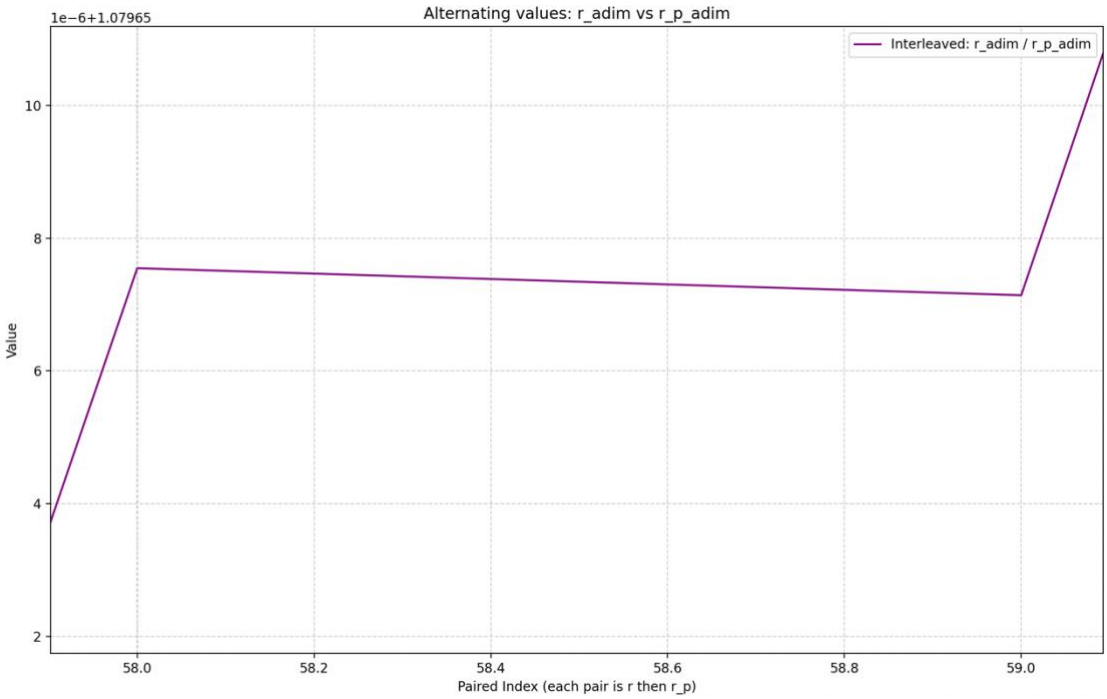

figure 30. comparison between r_adim and r_p_adim

As can be observed, following an increase in radius, there is a subsequent decrease due to the effects of perturbations, consistent with the loss of the thrust-related term.

The dimensionless velocity v exhibits a decreasing trend:

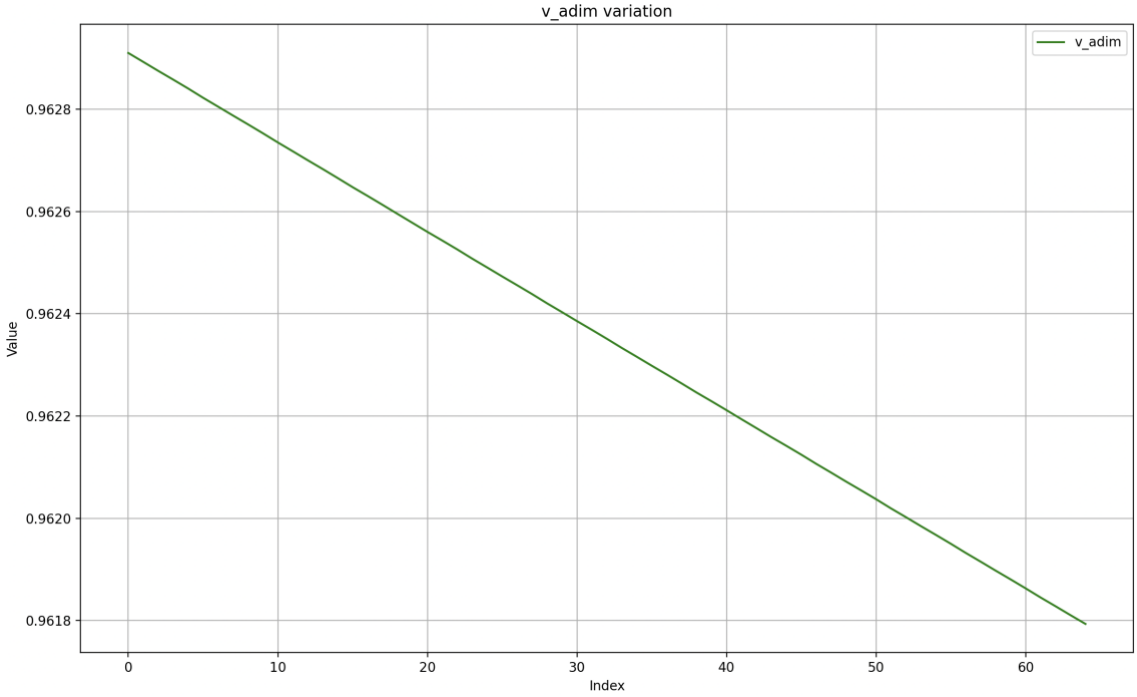

figure 31. velocity v variation

Similarly, the mass will follow an analogous trend since, in fact, propellant consumption occurs:

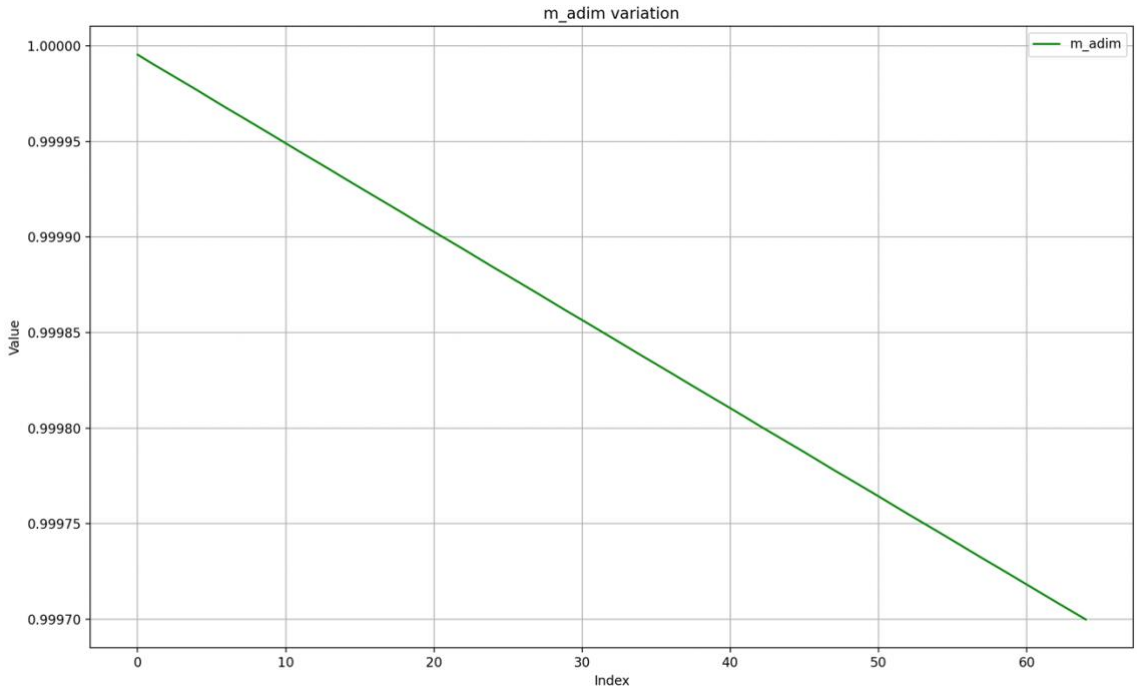

figure 32. mass variation

By exploiting the Tsiolkovsky equation, it is possible to estimate a preliminary cost of the manoeuvre:

$$\frac{m_f}{m_0} = e^{-\frac{\Delta V}{c}} \tag{27}$$

Deriving ΔV:

$$\Delta V = c \ln\left(\frac{m_0}{m_f}\right)$$

Substituting the values obtained from the simulation yields:

$$\Delta V = 0.008728827 \frac{km}{s}$$

Conclusions

This thesis aims to be a small starting point from which to begin evaluating, in an optimal manner, the movement of a satellite performing the active removal of debris.

Of particular interest may be considered the choices made regarding the operational scenario; indeed, the potential contribution of this study to the creation of a more sustainable space environment, with a consequent improvement in space access conditions, is key strength.

The objective of developing an optimisation and propagation code in Python that was as understandable and automated as possible can be considered achieved. The ability to perform manoeuvres of varying magnitudes at will, along with the presence of a graphical component that allowed visualising the effects of modifying parameters one at a time, were crucial for achieving convergence.

Considering future developments, there are numerous possibilities for improvement, as well as variations in the operational scenario.

With greater computational resources and advanced numerical stability techniques, it would have been possible to simulate the entire trajectory without dividing it into phases, reducing the time required to find initial values.

To increase the model's fidelity, it would be advisable to find a way to integrate ephemerides to obtain the actual positions of the Earth, Sun, and Moon.

Another operational case could involve reaching multiple debris pieces, with consequent optimisation of the path the satellite must follow during the various captures.

Bibliography

[1] P. Caraveo, Ecologia Spaziale, 2024.

[2] D. Liberzon, Calculus of Variations and Optimal Control Theory, 2012.

[3] G. Sarcletti, *Indirect optimization of low-thrust collision avoidance trajectories in LEO with bang-bang control laws,* 2024.

[4] A. Labarbuta, *Optimal Control Theory applied to interplanetary transfer for a Near-Earth Asteroid retrieval Mission,* 2024.

[5] C. Carone, *Low Thrust, Minimum-Propellant Optimization for Multi-Orbit Rendezvous with Uncooperative LEO Space Debris using Indirect Methods,* 2024.

[6] R. R. Bate, D. D. Mueller, J. E. White and W. W. Saylor, Fundamentals of Astrodynamics - second edition, 2020.

[7] J. M. Longuski, J. J. Guzmán and J. E. Prussing, Optimal Control with Aerospace Applications, 2014.

[8] N. K. Pavlis, S. A. Holmes, S. C. Kenyon and J. K. Factor, "The development and evaluation of the Earth Gravitational Model 2008 (EGM2008)," *J. Geophys. Res., B04406,* vol. 117, 2012.

[9] J. M. Picone, A. E. Hedin, D. P. Drob and A. C. Aikin, "NRLMSISE-00 empirical model of the atmosphere: Statistical comparisons and scientific issues," vol. 107(A12), no. 1468, 2002.

[10] L. Mascolo, *Low-Thrust Optimal Escape Trajectories from Lagrangian Points and Quasi-Periodic Orbits in a High-Fidelity Model,* 2023.

[11] ESA Space Debris Office, "ESA'S ANNUAL SPACE ENVIRONMENT REPORT," 2025.

[12] G7 leaders, "CARBIS BAY G7 SUMMIT COMMUNIQUÉ," 2021.

[13] ESA. [Online]. Available: https://www.esa.int/esearch?q=debris. [Accessed 17 07 2025].

[14] Istituto Nazionale di AstroFisica, [Online]. Available: https://sorvegliatispaziali.inaf.it/rifiuti-spaziali/. [Accessed 17 07 2025].

[15] Agenzia Spaziale Italiana, [Online]. Available: https://www.asi.it/lagenzia/risorse_informative/registro-nazionale-degli-oggetti-lanciati-nello-spazio/ambiente-spaziale-2/. [Accessed 17 07 2025].

[16] G. Kaldor. [Online]. Available: https://www.renewablematter.eu/rifiuti-spaziali-in-orbita-cosa-sono-soluzioni-. [Accessed 17 07 2025].

[17] ClearSpace, [Online]. Available: https://clearspace.today. [Accessed 17 07 2025].

[18] V. Fabiani, "infobuildenergia," [Online]. Available: https://www.infobuildenergia.it/approfondimenti/rifiuti-spaziali-detriti-futuro-sostenibile/. [Accessed 17 07 2025].

[19] National Geographic, [Online]. Available: https://www.nationalgeographic.it/la-nasa-ha-un-piano-per-rimuovere-i-rifiuti-spaziali-ma-potrebbe-gia-essere-troppo-tardi. [Accessed 17 07 2025].

[20] NASA, [Online]. Available: https://nssdc.gsfc.nasa.gov/nmc/spacecraft/display.action?id=1982-092A. [Accessed 17 07 2025].

[21] M. Wall, "SPACE.com," [Online]. Available: https://www.space.com/space-exploration/satellites/worlds-1st-wooden-satellite-arrives-at-iss-for-key-orbital-test. [Accessed 17 07 2025].

[22] Astroscale. [Online]. Available: https://astroscale.com/missions/adras-j/. [Accessed 17 07 2025].